

# Testing gravity with wide binaries

## 3D velocities and distances of wide binaries from Gaia and HARPS

R. Saglia<sup>1</sup>, L. Pasquini<sup>2,4</sup>, F. Patat<sup>2</sup>, H.-G. Ludwig<sup>3</sup>, R. Giribaldi<sup>4</sup>, I. Leao<sup>5</sup>, J. R. de Medeiros<sup>5</sup>, and Michael T. Murphy<sup>6,\*</sup>

<sup>1</sup> Max Planck Institute for Extraterrestrial Physics, Giessenbachstr. 85748 Garching, Germany  
e-mail: [saglia@mpe.mpg.de](mailto:saglia@mpe.mpg.de)

<sup>2</sup> ESO, Karl Schwarzschild Strasse 2, D-85478 Garching bei München

<sup>3</sup> Landessternwarte Zentrum für Astronomie der Universität Heidelberg, Königstuhl 12, 69117 Heidelberg, Germany

<sup>4</sup> INAF, Osservatorio Astrofisico di Arcetri, Largo E. Fermi, Firenze, Italy

<sup>5</sup> Departamento de Física, Universidade Federal do Rio Grande do Norte, 59078-970 Natal, RN, Brazil

<sup>6</sup> Centre for Astrophysics and Supercomputing, Swinburne University of Technology, Hawthorn, Victoria 3122, Australia.

Received, ; accepted,

### ABSTRACT

**Context.** Wide Binaries (WBs) are interesting systems to test Newton-Einstein gravity in low potentials. The basic concept is to verify whether the difference in velocity between the WB components is compatible with what is expected from the Newton law.

**Aims.** Previous attempts, based solely on Gaia proper motion differences scaled to transverse velocity differences using mean parallax distances, do not provide conclusive results. Here we add to the Gaia transverse velocities precise measurements of the third velocity component, the radial velocity (RV), in order to identify multiple stars, and to improve the reliability of the test by using velocity differences and positions in three dimensions.

**Methods.** We mine the ESO archive for observations of WBs with the high precision HARPS spectrograph, and use these observations to search for RV variations, that would indicate the presence of additional stars in the system. We use the HARPS spectra to determine accurate RV difference between the WB components, correcting the observed velocities for gravitational redshift and convective shift. We exploit the Gaia distance distributions to determine the projected and intrinsic separations  $s$  and  $r$  and the 3-dimensional velocity differences of the binaries.

**Results.** We retrieve 44 pairs observed with HARPS, most of them with numerous observations, spanning time baselines from week to years. A considerable fraction (27%) of these pairs show sign of multiplicity or are not suitable for the test, and 32 bona-fide WBs survive our selection. Their projected separation  $s$  is up to 14 kAU, or 0.06 parsec. The median renormalized unit weight error (RUWE) parameter for the final sample is of 0.975 (highest value 1.24) and the median RV variability is  $10 \text{ m s}^{-1}$  with standard deviation  $6 \text{ m s}^{-1}$ . Gaia RVs are on average smaller by only  $68 \text{ m s}^{-1}$  from those determined with HARPS, with an RMS dispersion of  $311 \text{ m s}^{-1}$ . We determine distances, eccentricities and position angles to reproduce the velocity differences according to Newton's law, finding reasonable solutions for all WBs but one, and with some systems possibly too near pericenter and/or at too high inclination.

**Conclusions.** We show that precise (and accurate) multiple RVs of WB candidates are a very powerful tool to make the WBs test of gravity more robust and reliable. These observations allow to minimize or eliminate one of the major limitations of previous tests, that is the presence of multiple systems, and make the comparison with theory straightforward, without the need to resort to complex simulations. Our (limited) number of WBs does not show obvious trends with separation or acceleration and is consistent with Newtonian dynamics. We are collecting a larger sample of this kind to robustly assess these results.

**Key words.** astrometry – parallaxes – proper motions – stars:binaries – stars:distances – stars: kinematics and dynamics

## 1. Introduction

General Relativity (GR) and its Newtonian limit stands as a cornerstone of physics, proven across a vast range of accelerations. However, in regions with extremely low accelerations, such as the outskirts of galaxies, the inclusion of an additional component, Dark Matter (DM) is required. While cold DM models effectively reproduce many astrophysical phenomena, the quest for the elusive particle responsible for DM underscores the importance of rigorously testing gravity against the predictions of GR. Wide Binaries (WB) have been proposed as an ideal laboratory for such scrutiny, given that their gravitational accelerations ( $\sim 10^{-10} \text{ m s}^{-2}$ ) closely resemble those found in the ex-

ternal regions of galaxies, see Hernandez et al. (2012). The underlying test is seemingly straightforward: assessing the degree to which WBs adhere to Kepler's laws. Given the exceedingly long period of their orbits, spanning many thousands of years, a complete reconstruction of the orbits is impossible. A statistical approach is instead employed, involving the measurement of velocity differences between the components of WBs and subsequent comparisons with simulations. The magnitude of this velocity difference, for a binary separation of 0.1 pc, or 20 thousand astronomical units (20 kAU), is  $50\text{--}200 \text{ m s}^{-1}$ , depending on eccentricity, which already sets the requirements on the velocity precision of this experiment. This test has been recently enabled by Gaia, thanks to its exquisite astrometry. Several groups have compiled samples of nearby WBs and executed the test using

\* Based on Archival ESO data

solely Gaia-derived data, focusing on 2D transverse velocities obtained from parallaxes, proper motions and separations (Hernandez et al. 2022, 2024; Pittordis & Sutherland 2019, 2023; Chae 2023; Banik et al. 2024; Chae 2024). These works are limited to use 2D velocities because, given the magnitude of the expected velocities involved, Gaia’s radial velocities (RVs) in general fall short of the required precision for this particular application. Chae (2025) improves on the situation by selecting the 312 WBs with the most precise available Gaia velocities, going beyond the transverse analysis. The outcomes of these investigations present a lack of consensus, with opposite conclusions drawn by different groups. While Hernandez et al. (2022, 2024); Chae (2023, 2024, 2025) suggest evidence indicating a departure from GR for separations exceeding approximately 3 kAU, Pittordis & Sutherland (2019, 2023); Banik et al. (2024) argue that no deviations from GR are detected. As a reference, at 3 kAU separation, the velocity difference expected according to Newton law for two solar mass stars in circular orbits is (see below)  $V = 770 \text{ m s}^{-1}$  and the acceleration  $1.3 \times 10^{-9} \text{ m s}^{-2}$ . The ongoing discussion underscores the complexity of the matter, which can be attributed to several factors, all arising from the absence of precise RVs. A primary complicating factor is the presence of triple systems. When one of the two components within the WBs is a binary system itself (with a separation too small to be resolved by Gaia), the resulting velocity becomes inflated (Clarke 2020). Thus, it is imperative to incorporate triple systems into simulations involving the WB population. Transitioning from 3D orbits to 2D projections introduces an additional layer of uncertainty. Furthermore, the potential lack of physical association among some WBs in the sample could contribute to contamination. These effects persist, despite various precautions taken by researchers in sample creation to minimize them. The divergence in conclusions among the studies primarily stems from simulating the parent WB population with different selections criteria, magnifying the need for more accurate observational data.

As suggested by Pittordis & Sutherland (2018), we overcome these limitations by searching in the ESO archive for HARPS (Mayor et al. 2003) observations of systems classified in literature as wide binaries, finding 44 systems in the archive, to obtain accurate measurements of their third (radial) velocity dimension, to exclude the presence of triple systems and to make a full 3D velocity comparison. HARPS observations typically span long (up to several years) time baseline, and thanks to the excellent RV precision (typically better than  $10 \text{ m s}^{-1}$ ) of this instrument, it is possible to determine whether a hidden companion contaminates the system. Moreover, we exploit the information coded by the Gaia parallaxes and their errors to estimate the probability distributions of the WB distances and intrinsic separations.

The paper is organized as follows. Section 2 explains the method used, Sect. 3 describes the sample. Section 4 describes the modeling, considering first the relevant Newtonian equations and the geometric setup in Sect 4.1, then the determination of distances and the scaling of velocity differences in Section 4.2, and finally presenting the Newtonian solutions in Section 4.3. Section 5 discusses the obtained results. Section 6 draws our conclusions. The Appendix A describes the discarded pairs.

## 2. Method

Comparing the observations of WBs with Newton theory is in principle simple, as it requires to measure the distribution of observed velocity differences between the components of the WBs ( $V_{\text{ra}}$ ,  $V_{\text{dec}}$ ,  $V_{\text{rad}}$ ) and their separation, and to compare the results of the observations with theoretical predictions. In practice, the

exceedingly long orbital periods and the small velocity difference expected in WBs make the process more complex and also set some limitations: for instance only angular separations on the sky are known with precision, and the full 3D orbit cannot be recovered. In the following we recap the steps used in the process and how they have been applied here or in the past.

Measure the separation: thanks to Gaia, the separation between the stars can be computed very precisely by using Gaia coordinates and parallaxes. Several authors (Pittordis & Sutherland 2019; Chae 2024, 2025) have argued that the exquisite Gaia parallaxes are not precise enough to compute the separation in 3D, because the residual error in the stellar distances is comparable to the stars’ separation. Then projected separations  $s$  are computed, by assuming that both stars lie at the distance of the system, obtained by averaging the parallaxes, weighted for their parallax error. The uncertainty on the separation  $s$  is better than 0.1%. In Sect. 4.2 we describe how we can go beyond this approach and estimate the intrinsic separation  $r$  of the systems.

Remove not-suitable systems: the main cause of contamination of WBs samples is the presence of multiple systems, that will heat the velocity difference between the WBs components. Chance alignment, though more rare in systems with separations below 1 parsec (El-Badry et al. 2021) must also be considered. As far as multiple systems are concerned, it is important to recall that these potential intruders are close companions of one of the stars unresolved by Gaia. The main tools we use to determine close companions are the variability of multiple precise RVs and the renormalized unit weight error (RUWE) parameter of Gaia. Kervella et al. (2022) argue that a RUWE value of around 1.0 is expected for a single-star astrometric solution. In contrast, a value significantly larger than 1.0, typically larger than 1.4, could indicate a non single source or one problematic for the astrometric solution. Given the rather good agreement between the HARPS and Gaia RVs (see below), a very large difference (several  $\text{km s}^{-1}$ ) between HARPS and Gaia RVs also indicates the presence of a companion. Penoyre et al. (2022a) noted that RUWE values of less than 1.25 could still be multiple systems where the inner periods are a significant multiple of the GAIA baseline observation period (34 months for DR3). However, the fraction of binaries that can significantly survive a RUWE=1.25 threshold is considerable only for orbital periods of a few decades and drops at a few percent for binaries with 100 yr period. But we are able to identify such systems (provided they are not in extreme face-on configurations) through multiple HARPS observations. As an example, a  $2M_{\odot}$  binary at a separation of 20 AU has an orbital period of 63 yr; observing the system with HARPS one year apart allows one to detect the expected variations in the radial velocity differences (more than  $30 \text{ m s}^{-1}$  in 84% of the cases for an eccentricity of 0.6 and random orientations). Only binary #27 of our sample has an extremely low (0.02) radial to tangential velocity ratio (see Sect. 5).

It is not obvious how to establish a priori a firm criterium on RV variability for considering a star a close binary. RV variability may in fact depend on several factors, such as: precision of the measurements, presence of companions, rotational velocity and spectral type (Bouchy et al. 2001), stellar activity and pulsations. The typical precision of the HARPS single exposure is of a few  $\text{m s}^{-1}$ , but no correction has been adopted for long term instrumental drifts, nor whether different versions of the pipeline have been used to measure the RVs (Barbieri 2024). For instance, if an object has been observed with HARPS before and after the fiber change (Lo Curto et al. 2015), a zero point offset of about  $15 \text{ m s}^{-1}$  is expected for solar stars. The RV variability induced by stellar activity, either due to rotational modulation or to

long term stellar cycles, is difficult to estimate, but all our WBs are reasonably old ( $> 1$  Gyrs). When considering the  $50 \text{ m s}^{-1}$  RV modulation measured in the young ( $\sim 8 \times 10^8$  yrs) Hyades stars caused by rotational modulation (Saar & Donahue 1997) and that activity decreases exponentially with age in the first two Gyrs, to reach a level compatible to the Sun (Pace & Pasquini 2004), we estimate that rotational modulation should contribute to RV variability not more than a dozen  $\text{m s}^{-1}$  (peak to peak), as observed by HARPS in the Sun (Haywood et al. 2016). Long term cycle RV variability (equivalent to the 11-yr solar cycle), which is relevant for observations spanning a time baseline of years, is also poorly characterized, but the variations of the solar RV over almost a decade have been measured to less than  $5 \text{ m s}^{-1}$  with HARPS (Lanza et al. 2016). Considering all these factors, a long term RV velocity variability of the order of  $10 \text{ m s}^{-1}$  if fully compatible with a binary system. Only larger values may be seen as a signature of a third component.

The Gaia RUWE parameter is also a powerful tool to identify binaries (Belokurov et al. 2020) and different maximum values have been suggested to limit the sample to single stars, with Lindgren et al. (2018) suggesting  $\text{RUWE} < 1.4$  for DR2 data and Penoyre et al. (2022b) finding that  $\text{RUWE} = 1.25$  is the most extreme value expected from stochastic scatter of single stars. As a reference, our final sample has a median RUWE of 0.975 and the highest RUWE is 1.24.

To find systems aligned by chance, we adopt chemical composition as primary indicator: the high resolution spectra obtained for the RV measurements were used to determine precise stellar parameters and chemical composition (Spina et al. 2021). In our sample (see next section) we discarded as alignment chances those systems whose components  $[\text{Fe}/\text{H}]$  differ by more than 3 times their associated uncertainty in  $[\text{Fe}/\text{H}]$ .

In order to minimize the contamination by proper motion pairs, we excluded cases younger than 1 Gyrs and/or belonging to known clusters. Common proper motion pairs have in fact a reasonable high probability to survive in the first Gyr of their life (Jiang & Tremaine 2010).

In the absence of firm physical limits on velocity variability and RUWE parameter to be imposed a priori, we opted to clean the original sample in an interactive way: we used the precise HARPS RVs to individuate stars showing large RV variations, eliminating WBs with RV variability exceeding  $100 \text{ m s}^{-1}$  and with high RUWE ( $> 1.4$ ). We carefully looked at the remaining stars, and in some doubtful case, we excluded stars that had both high RV variability and a large RUWE parameter. When the HARPS RV measurement differs substantially from Gaia (several  $\text{km s}^{-1}$ ), we also remove the star as a likely binary. We consider our selection process as conservative (cfr. next section and Appendix A, where we motivate our decisions).

Compute the 3D velocities: the 3D velocity difference  $V_{\text{tot}}$  has two components: the astrometric component (transverse or tangential velocity) and the RV. The tangential velocity difference is usually computed by scaling the Gaia proper motions and errors with the mean distance of the system. In Sect. 4.2 we go beyond this simplified approach by exploiting the distance probability distributions delivered by Gaia. We compute velocities in the right ascension and declination direction by scaling the proper motions and relative errors with the assumed distances of the two stars separately before taking their differences.

Since the two stars forming a WB have not the same physical parameters, we need to obtain accurate RVs, properly correcting the observed shifts. To compute the absolute RV we used the process adopted in Leão et al. (2019). These authors showed that HARPS observed shifts, corrected for gravitational redshift and

convective motions, agree with astrometric velocities to better than  $40 \text{ m s}^{-1}$ . A similar method has been applied to the  $\alpha$  Cen system by Kervella et al. (2017) with a comparable accuracy. From the observed HARPS Cross Correlation Function (CCF) velocities we subtracted the gravitational redshift and the correction for convective shift. Both quantities depend on basic stellar parameters. Gravitational redshift depends on the stellar mass and radius, while the convective shift is computed by using 3D atmospheric models that depend mostly on stellar effective temperature and gravity (Ludwig et al. 2009). The metallicity of our sample stars is sufficiently close to solar, that only solar metallicity atmospheric models can be used. In summary, the RV of each star  $i$  has been computed as  $RV_i = V_{\text{HARPS},i} - GR_i - V_{\text{con},i}$ , where  $V_{\text{HARPS},i}$  is the HARPS velocity shift measured by fitting the mask cross-correlation function and determined to some  $\text{m s}^{-1}$  precision,  $GR_i$  is the gravitational redshift and  $V_{\text{con},i}$  is the convective (blue) shift estimated by cross-correlating the synthetic spectra generated with 3D models (Ludwig et al. 2009; Leão et al. 2019) with the same digital mask used for the observations.

As far as the associated error to  $RV_i$ , the systematic uncertainties on the gravitational redshifts cancel out when the velocity differences of the pairs are computed, given that masses and radii of the pairs are never too dissimilar and are computed with the same method. The uncertainty on the convective shift correction is not precisely known, and it is estimated of the order of a few tens of  $\text{m s}^{-1}$ . The uncertainty of  $40 \text{ m s}^{-1}$  obtained for the Hyades stars by Leão et al. (2019) and the estimated error of Kervella et al. (2017) empirically confirm this estimate. This factor is the main source of error in the RV measurements. The impact of the gravitational redshift and convective shift on the RV difference of the pair is in all but one WB small, but becomes relatively more important, the smaller the relative velocities of the WB are.

### 3. Sample

The HARPS science products available in the ESO archive contain, in addition to the spectra, also the computed RV, together with the mask used for the cross-correlation and other characteristics of the CCF. An interface has been recently built to retrieve the RVs and other CCF parameters from the catalogue of HARPS observations (Barbieri 2024). In the past 20 years, several WB candidates have been observed with HARPS in the framework of different programs, either dedicated to the search of exoplanets or to study the detailed chemical composition of WBs (Spina et al. 2021). The list of Spina et al. has been the main input for the HARPS search, that has produced 44 WB candidates.

Most of the stars have been analyzed differentially obtaining very precise effective temperature, gravity and abundance determinations. Spina et al. (2021) quote errors of 10 K or less on temperatures, 0.2 dex or less on  $\log(g)$  and 0.03-0.06 dex on  $[\text{Fe}/\text{H}]$ . The tiny abundance differences between the pairs might be the product of evolutionary effects like diffusion, or induced by the presence of exo-planetary systems or debris contamination (Spina et al. 2021) rather than evidence of different birthplace. Therefore, we have first cleaned the sample of binaries for stars with a  $[\text{Fe}/\text{H}]$  abundance difference larger than 3 times the  $[\text{Fe}/\text{H}]$  uncertainty in their components. One pair was discarded with this step. All the final pairs have differences in  $[\text{Fe}/\text{H}]$  abundance of less than 0.1 dex but two: binaries #12 and #21, that have the largest uncertainty in their  $[\text{Fe}/\text{H}]$  determination. The mean difference in  $[\text{Fe}/\text{H}]$  is -0.01 dex with 0.06 dex RMS. We

also used the estimated stellar ages and their 95% confidence levels (determined while computing the stellar masses and radii, see below) to verify that the stars are older than 1 Gyr, that the age estimates for the components of the same WB are compatible within the errors. In this step one pair was eliminated: with an age estimate of 700 Myr and belonging to the Hyades. No other pair could be associated to a cluster, nor any other young star is left in the final sample. The average difference between the ages of the pairs is 0.3 Gyr with 3 Gyr RMS.

The sample is heterogeneous in terms of number of observations and time baseline. All stars but three have several HARPS observations, ranging from 2 to more than 90, covering a time-line that spans from weeks to more than 10 years. Since the majority of the stars has multiple HARPS observations, we are able to perform the cleaning using RV variability. RVs are read off the Barbieri (2024) catalogue, inspected, and also compared with the Gaia RVs (Katz et al. 2023). The nature of our WBs requires some caution in using the catalogue: some of the components of the WBs are so close on the sky that the 3.6m telescope coordinates do not help in discriminating which star has been observed, and it is risky to rely only on the data header, so the observations must be carefully scrutinized. In those few doubtful cases the observations (RV, width of the CCF) have been inspected and they provide a clear information on which star has been observed. In one case we found an unexplained shift of several  $\text{km s}^{-1}$  in the HARPS catalogue, that, after direct inspection of the spectra, was not present in the original data. This is to emphasize that for this sample we could not use the catalogue blindly, but a manual cleaning has been necessary. For each star we measured the mean RV and its RMS. For three stars, HARPS observations are not available (WASP-94 B, HIP47839, HD135101B): for them we adopted the difference in RV with respect to the other binary component as measured by Gaia, with an associated RV error of  $300 \text{ m s}^{-1}$  (see below). For HD135101A, out of 71 observations, two show a different RV, and CCF width. We attributed these observations to the companion, HD135101B. The RUWE values were finally used, as explained above.

After the cleaning process, 32 binaries (64 stars, or 73%) out of 44 survived the selection. The Gaia parameters (right ascension, declination, parallax, proper motions and RUWE values) of the 64 stars are given in Table B.1. The stellar properties (age, effective temperature, gravity, metallicity, mass, radius, gravitational redshift, convective shift, mask and number of HARPS observations, RV) are given in Table B.2. Temperature, gravity and metallicity come from (Spina et al. 2021); the missing values are listed as  $9999 \pm 9999$ ; they are available from Perdelwitz et al. (2024), but we do not use them for consistency. The gravity values given in italics are Gaia values. Age, mass, radius and convective shifts are computed as described below. All the binaries are limited to on-sky separations of less than 20 kAU. The discarded pairs are described in the Appendix A, together with the rejection reason.

The median RV variability for the final sample is  $10 \text{ m s}^{-1}$  with  $6 \text{ m s}^{-1}$  RMS. Some of the stars with a high RV variability, such as HD20782 or HD106515A, are known to host massive exo-planets, and this clearly enhances their stellar RV variability. None of our stars show a RMS larger than  $29 \text{ m s}^{-1}$  (HD106515A).

Summarizing the results of our cleaning process, we can confirm that *for this sample of observations* a maximum RUWE value of 1.25, and, a long-term RV variability of 10 with  $6 \text{ m s}^{-1}$  RMS would have been a priori good choices to select pairs composed by single stars.

For most stars precise stellar parameters ( $T_{\text{eff}}$ ,  $\log(g)$ , chemical composition) are given in (Spina et al. 2021), and have been determined by spectroscopy, applying a differential, line - to - line, technique that maximizes the precision. These parameters have been adopted as input to determine stellar masses, radii and ages using the 'param 1.4' interface (da Silva et al. 2006; Rodrigues et al. 2014, 2017)<sup>1</sup> and PARSEC isochrones from Bressan et al. (2012). For the stars without spectroscopic  $\log(g)$  (listed in italics in Table B.2) and/or metallicities from Spina et al. (2021), we used the version 1.3 that accepts magnitudes and parallaxes. For the stars with spectroscopic  $\log(g)$  the two methods agree within the estimated errors. The only difference between the published data and those used in this work is that we set the minimum  $T_{\text{eff}}$  uncertainty to 30 K (for most stars the published uncertainty is much smaller), in order to allow the evolutionary code to converge, because the algorithm may not do so for  $T_{\text{eff}}$  uncertainties of a few K. The derived stellar masses and radii are used to compute the gravitational redshifts; the convective shift corrections are computed using the values of  $\log(g)$  listed in Table B.2. They differ slightly (within the errors) from the values derived from the stellar masses and radii given in Table B.2.

Since what matters are the relative shifts and the relative gravitational redshifts between the two WB components, it is more important that the stellar parameters are on the same scale rather than their accuracy is on an absolute scale. We estimate from the 95% confidence levels quoted by 'param' and the comparison between the versions 1.3 and 1.4 that the systematic error affecting the total masses of the binaries is at most 10%.

Comparing the HARPS (not corrected) and Gaia RV we find that the zero point differs by a median value of  $68 \text{ m s}^{-1}$ , with  $311 \text{ m s}^{-1}$  RMS; when comparing our final RVs (corrected for gravitational redshift and convective shift) with Gaia, the median zero point difference is  $-37 \text{ m s}^{-1}$ , with  $300 \text{ m s}^{-1}$  RMS. This spread is in line with the expected precision of the Gaia RV. The HARPS RVs median values, not corrected for GR and convective shift, are given in Table B.2.

## 4. Modeling

### 4.1. Newtonian orbits and Geometry

We define the geometry and the set of equations used to reproduce the measured velocities assuming Newtonian dynamics, similar to the approach of Chae (2023). Here we adopt lower case symbols to label velocities and angles; upper case symbols are used for the quantities determined in Sect. 4.2. Figure 1 shows the plane of the orbit. The reduced orbit is an ellipse with eccentricity  $e$ . The distance  $r$  to its focus in terms of the semi-major axis  $a$  depends on the actual position (or phase) on the orbit given by the angle  $\phi - \phi_0$ :

$$\frac{r}{a} = \frac{1 - e^2}{1 + e \cos(\phi - \phi_0)}; \quad (1)$$

$r/a$  can assume values between  $1 - e$  (pericenter for  $\phi - \phi_0 = 0$ ) and  $1 + e$  (apocenter for  $\phi - \phi_0 = \pi$ ):

$$1 - e \leq r/a \leq 1 + e; \quad (2)$$

$r/a$  is equal to 1 when  $\cos(\phi - \phi_0) = -e$ . The relative velocity of the binary expected from Newtonian dynamics is:

$$v(r) = \sqrt{\frac{GM}{r} \left(2 - \frac{r}{a}\right)} = v_N \sqrt{2 - \frac{r}{a}}, \quad (3)$$

<sup>1</sup> <https://stev.oapd.inaf.it/cgi-bin/param>

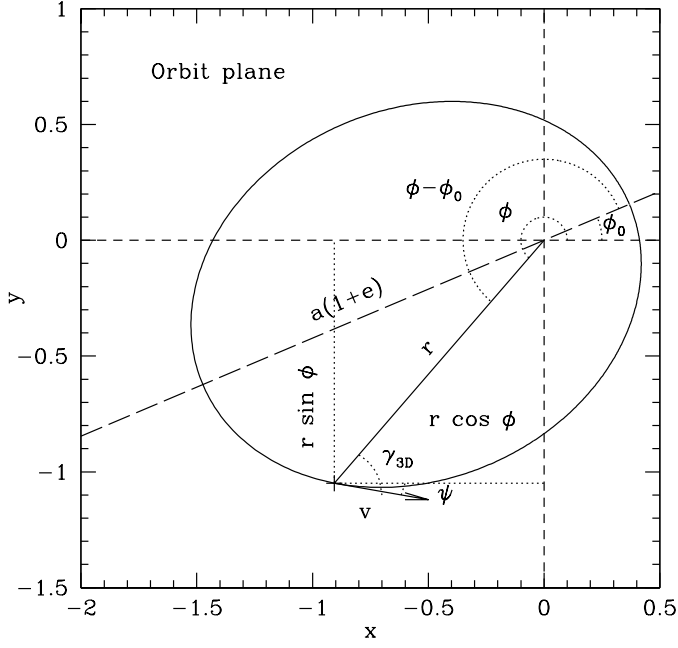


**Fig. 1.** The plane of the orbit. The axis  $x$  is defined by the intersection of the plane of the orbit and the plane of the sky. The periastron is at an angle  $\phi_0$  from the  $x$  axis;  $\phi$  is the angle between the  $x$  axis and the position on the orbit;  $\psi$  is the angle between the  $x$  axis and the velocity vector  $v$ . The angle between the position and velocity vectors is  $\gamma_{3D}$ .

where  $M = M_1 + M_2$ ,  $a$  is the semi-major axis of the orbit,  $e$  the eccentricity of the orbit,  $v_N = \sqrt{\frac{GM}{r}}$  is the velocity expected for  $e = 0$  and the acceleration is  $A_N = GM/r^2$ . The period of the orbit is  $T_N^2 = \frac{4\pi^2}{GM}a^3$ . The fractional time  $\Delta t/T_N$  spent between phase  $\phi_1$  and  $\phi_2$  is given by:

$$\Delta t/T_N = \int_{\phi_1}^{\phi_2} \frac{d\phi'}{(1 + e \cos \phi')^2} / \int_0^{2\pi} \frac{d\phi'}{(1 + e \cos \phi')^2}. \quad (4)$$

Fig. 2 shows the projection on the sky. The angle between the plane of the orbit and the plane of the sky is the inclination angle  $i$ . The true separation  $r$  of the binaries given its projected separation  $s$  on the sky is:

$$r = \frac{s}{\sqrt{\cos^2 \phi + \cos^2 i \sin^2 \phi}}, \quad (5)$$

where  $r \geq s$ ,  $\phi$  is the angle between the axis  $x$  defined by the intersection of the plane of the orbit and the plane of the sky and the position on the orbit. The periastron is at an angle  $\phi_0$  from the  $x$  axis. When  $i = 0$  the orbit is face-on and  $r = s$ . When  $i = \pi/2$  the orbit is edge-on and  $s/r = \cos \phi$ ; when  $\phi = \pi/2$  or  $\phi = 3\pi/2$  the position of the orbit is orthogonal to the intersection of the plane of the orbit and the plane of the sky. Eq. 5 can be rewritten to express  $\phi$  as a function of  $s/r$  and  $i$ :

$$\cos^2 \phi = \frac{(s/r)^2 - \cos^2 i}{\sin^2 i}, \quad (6)$$

from which one finds that the minimum possible inclination angle has  $\cos i_{\min} = s/r$ .

The component  $v_{\text{rad}}$  of the relative velocity  $v$  along the line of sight is given by:

$$v_{\text{rad}} = v \sqrt{1 - \cos^2 \psi - \cos^2 i \sin^2 \psi} = v \sin \psi \sin i, \quad (7)$$

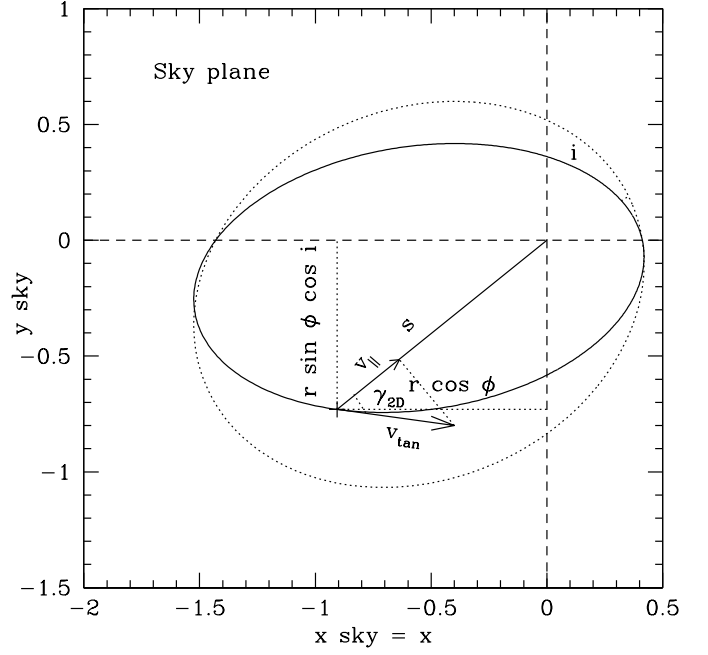


**Fig. 2.** The orbit projection on the sky. The angle between the position and velocity vectors on the sky is  $\gamma_{2D}$ .

where

$$\psi = \arctan \left( -\frac{\cos \phi + e \cos \phi_0}{\sin \phi + e \sin \phi_0} \right). \quad (8)$$

Since  $\sin \psi = v_{\text{rad}}/v / \sin i \leq 1$ , this implies that the inclination angle has to be larger than  $i_{\min} = \arcsin v_{\text{rad}}/v$ .

The component  $v_{\text{tan}}$  on the sky is then  $v_{\text{tan}} = \sqrt{v^2 - v_{\text{rad}}^2}$ . The ratio:

$$\frac{v_{\text{rad}}}{v_{\text{tan}}} = \frac{\sin \psi \sin i}{\sqrt{1 - \sin^2 \psi \sin^2 i}} \quad (9)$$

is small for nearly face-on orbits with  $i \approx 0^\circ$  and is approximately equal to  $\tan \psi$  for nearly edge-on orbits with  $i \approx 90^\circ$ . In this case values of  $\psi \approx 0$  also produce  $v_{\text{rad}}/v_{\text{tan}} \approx 0$ .

The angle  $\gamma_{2D}$  between the position vector projected on the sky and the velocity vector projected on the sky is given by:

$$\cos \gamma_{2D} = \frac{e \cos^2 i \cos \phi_0 \sin \phi - \cos \phi (e \sin \phi_0 + \sin^2 i \sin \phi)}{d \sqrt{\cos^2 \phi + \cos^2 i \sin^2 \phi}} \quad (10)$$

where

$$d = \sqrt{\cos^2 i (e \cos \phi_0 + \cos \phi)^2 + (e \sin \phi_0 + \sin \phi)^2}, \quad (11)$$

see Eq. A1 of Hwang et al. (2022). For face-on ( $i = 0$ ) orbits  $\gamma_{2D} = \gamma_{3D}$  (see Eq. 13); for edge-on ( $i = 90^\circ$ ) orbits,  $\gamma_{2D}$  can be 0 or  $180^\circ$ . The velocities parallel and orthogonal to the position vector projected on the sky are:

$$v_{\parallel} = v_{\text{tan}} \cos \gamma_{2D}; v_{\perp} = v_{\text{tan}} \sin \gamma_{2D}, \quad (12)$$

respectively. Finally, the angle  $\gamma_{3D}$  between the (tri-dimensional) position and velocity vectors is given by:

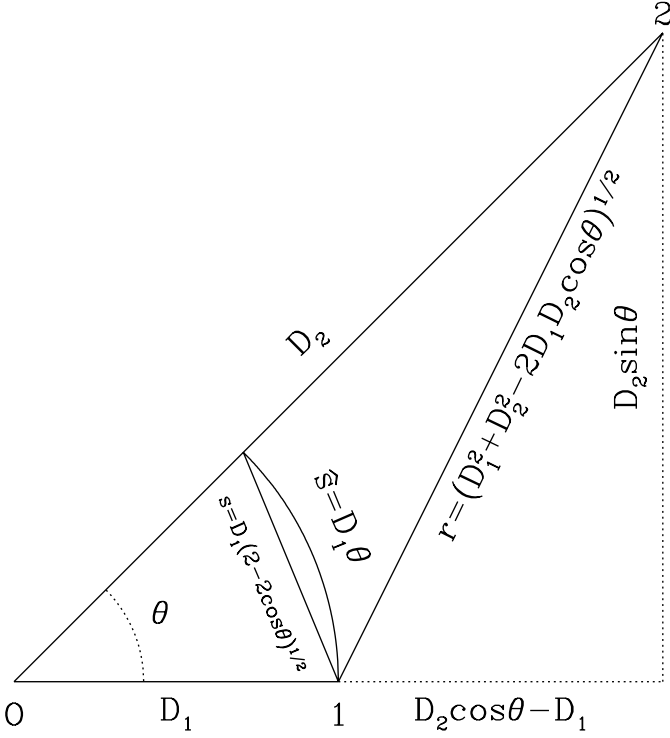


**Fig. 3.** The geometry of the binary system from the observer's point of view.

$$\cos \gamma_{3D} = \frac{e \sin(\phi - \phi_0)}{\sqrt{1 + e^2 + 2e \cos(\phi - \phi_0)}}. \quad (13)$$

The maximum value that  $\cos \gamma_{3D}$  can reach is  $e$  at  $\cos(\phi - \phi_0) = -e$ . Both  $\cos \gamma_{2D}$  and  $\cos \gamma_{3D}$  change sign when the signs of both angles  $\phi_0$  and  $\phi$  are changed.

#### 4.2. Distances and velocities

Figure 3 shows the geometric configuration of the binary system from the observer's point of view, where we have assumed that star 1 (with mass  $M_1$ ) is at a distance  $D_1$  and star 2 (with mass  $M_2$ ) at a distance  $D_2$  with  $D_1 < D_2$ . For our sample of binaries the angle  $\theta$  between the directions of the two stars of the pair is at most 5.4 arcmin, or 0.00157 radians, with a median value of 18.9 arcsec, or  $10^{-4}$  radians (see Table B.3). This allows us to set the chord  $s$  to the length of the arc  $\hat{s}$  and simplify the projected distance on the sky of the binary to

$$s = \min(D_1, D_2)\theta \quad (14)$$

and the true distance between the stars:

$$r = \sqrt{(D_2 - D_1)^2 + D_1 D_2 \theta^2}. \quad (15)$$

The distances  $D_1$  and  $D_2$  follow approximately Gaussian distributions with means  $\bar{D}_1 = 1/p_1$  pc and  $\bar{D}_2 = 1/p_2$  and dispersions  $\delta D_1 = \bar{D}_1 \delta p_1 / p_1$  and  $\delta D_2 = \bar{D}_2 \delta p_2 / p_2$ , where  $p_1$  and  $p_2$  are the measured parallaxes and their respective errors  $\delta p_1$  and  $\delta p_2$  (see Table B.1). Then  $s$  and  $r$  are given by the Eqs. 14 and 15. We define  $D_{\text{mean}} = (D_1 + D_2)/2$ ,  $\bar{D}_{\text{mean}} = (\bar{D}_1 + \bar{D}_2)/2$  and  $s_{\text{mean}} = \theta D_{\text{mean}}$ ,  $\bar{s}_{\text{mean}} = \theta \bar{D}_{\text{mean}}$ . We compute  $\bar{s}$  inserting  $\min(\bar{D}_1, \bar{D}_2)$  in Eq. 14 and  $\bar{r}$  inserting  $\bar{D}_1$  and  $\bar{D}_2$  in Eq. 15. We

show in Sect. 5 that for our sample  $\bar{r}$  overestimates  $r$  by more than one order of magnitude.

The relative velocities of the binary in the right ascension and declination directions are derived by scaling the proper motions of the pair  $(pm\alpha_1, pm\delta_1)$  and  $(pm\alpha_2, pm\delta_2)$  with the distances:

$$V_{\text{ra}} = D_2 pm\alpha_2 - D_1 pm\alpha_1, \quad (16)$$

$$V_{\text{dec}} = D_2 pm\delta_2 - D_1 pm\delta_1. \quad (17)$$

In analogy with what written above, we define  $\bar{V}_{\text{ra}} = \bar{D}_2 pm\alpha_2 - \bar{D}_1 pm\alpha_1$ ,  $\bar{V}_{\text{dec}} = \bar{D}_2 pm\delta_2 - \bar{D}_1 pm\delta_1$ ,  $\bar{V}_{\text{ra,mean}} = (pm\alpha_2 - pm\alpha_1)\bar{D}_{\text{mean}}$ ,  $\bar{V}_{\text{dec,mean}} = (pm\delta_2 - pm\delta_1)\bar{D}_{\text{mean}}$ . Chae (2025, 2024) use  $\bar{V}_{\text{ra,mean}}$  and  $\bar{V}_{\text{dec,mean}}$  in their analysis.

The errors on  $V_{\text{ra}}$  and  $V_{\text{dec}}$  are in most of the cases less than 0.1%:

$$\delta V_{\text{ra}} = \sqrt{D_2^2 \delta pm\alpha_2^2 + D_1^2 \delta pm\alpha_1^2}, \quad (18)$$

$$\delta V_{\text{dec}} = \sqrt{D_2^2 \delta pm\delta_2^2 + D_1^2 \delta pm\delta_1^2}. \quad (19)$$

The relative velocity of the binary projected on the plane of the sky is:

$$V_{\text{tan}} = \sqrt{V_{\text{ra}}^2 + V_{\text{dec}}^2}. \quad (20)$$

The angle between the vector connecting the pair and the vector of velocities on sky is:

$$\cos \Gamma_{2D} = \frac{(\alpha_1 - \alpha_2) \cos \bar{\delta} V_{\text{ra}} + (\delta_1 - \delta_2) V_{\text{dec}}}{\sqrt{(\alpha_1 - \alpha_2)^2 \cos^2 \bar{\delta} + (\delta_1 - \delta_2)^2 V_{\text{tan}}^2}}, \quad (21)$$

where  $(\alpha_1, \delta_1)$  and  $(\alpha_2, \delta_2)$  are the RA and DEC coordinates of the pair and  $\bar{\delta} = (\delta_1 + \delta_2)/2$ . Then, the components of  $V_{\text{tan}}$  parallel and orthogonal to the separation vector are

$$V_{\parallel} = V_{\text{tan}} \cos \Gamma_{2D}; V_{\perp} = V_{\text{tan}} \sin \Gamma_{2D}. \quad (22)$$

We compute the errors  $\delta V_{\parallel}$ ,  $\delta V_{\perp}$ ,  $\delta V_{\text{tan}}$  and  $\delta \Gamma_{2D}$  by generating 100 Monte Carlo samples of  $V_{\text{ra}}$  and  $V_{\text{dec}}$  and computing the RMS of the generated samples of  $V_{\parallel}$ ,  $V_{\perp}$ ,  $V_{\text{tan}}$  and  $\Gamma_{2D}$ . The errors reported in Table B.4 are on average 2% for  $V_{\text{ra}}$  and  $V_{\text{dec}}$ . The error on the angle  $\Gamma_{2D}$  is on average 0.3 degrees.

The (distance independent) component of the relative velocity of the binary along the line of sight is:

$$V_{\text{rad}} = RV_2 - RV_1 \quad (23)$$

with an error

$$\delta V_{\text{rad}} = \sqrt{\delta RV_2^2 + \delta RV_1^2 + \delta V_{\text{cor}}^2}, \quad (24)$$

where  $\delta RV_1$  and  $\delta RV_2$  are the errors on the measured RVs and  $\delta V_{\text{cor}} = 40 \text{ m s}^{-1}$  takes into account the uncertainties in the gravitational redshift and convection motion corrections. On average,  $\delta V_{\text{rad}}$  is on the order of  $50 \text{ m s}^{-1}$ , except for the three pairs (#13, #15, #28) where no HARPS measurements for one of the binaries are available. Therefore,  $\delta V_{\text{rad}}$  is one order of magnitude larger than  $\delta V_{\text{tan}}$ .

We reverse the sign of the coordinate differences,  $V_{\text{rad}}$ ,  $V_{\text{ra}}$ , and  $V_{\text{dec}}$  if  $D_1 > D_2$ , which does not change the sign of  $\Gamma_{2D}$ .

The total relative velocity of the binary is:

$$V_{\text{tot}} = \sqrt{V_{\text{tan}}^2 + V_{\text{rad}}^2}, \quad (25)$$

from which we compute the ratio  $R = V_{\text{rad}}/V_{\text{tot}}$ . Its error  $\delta R$  is determined by generating 100 Monte Carlo samples of  $R$  and computing their RMS. Finally, the angle between the (tri-dimensional) vector connecting the pair and the vector of velocity difference is:

$$\cos \Gamma_{3D} = \frac{s V_{\text{tan}} \cos \Gamma_{2D} \pm \sqrt{r^2 - s^2} V_{\text{rad}}}{r V_{\text{tot}}}, \quad (26)$$

where the + applies if  $D_2 > D_1$  and the – if  $D_2 < D_1$ . We determine the error on  $\Gamma_{3D}$  by generating 100 Monte Carlo samples of  $\Gamma_{3D}$  and computing their RMS. Since  $\delta V_{\text{tan}}$  is smaller than  $\delta V_{\text{rad}}$ , the angle  $\Gamma_{2D}$  is (much) better determined than  $\Gamma_{3D}$ . Indeed, the error on the angle  $\Gamma_{3D}$  is on average 4 degrees.

### 4.3. Best-fitting Newtonian solutions

Given the small errors affecting both measured velocities and masses of our WBs, we expect to reduce the uncertainty on the 3D separations of the binaries by searching for Newtonian orbits that reproduce the observed relative positions and velocities as much as possible. We sample the parameter space  $D_1, D_2, i, \phi, e, \phi_0$  to find the best matches between  $(V_{\text{rad}}, V_{\parallel}, V_{\perp})$  and  $(v_{\text{rad}}, v_{\parallel}, v_{\perp})$  as follows. We start by sampling the distances  $D_1$  and  $D_2$  according to their Gaussian distributions set by the mean distances  $\bar{D}_1, \bar{D}_2$  and errors  $\delta D_1, \delta D_2$  derived from the parallaxes listed in Table B.1. We select (if they exist) the pairs of distances that deliver separations  $r$  that allow for maximum velocities  $v_{\text{max}} = v_N \sqrt{2}$  (see Eq. 3) larger than the total velocity  $V_{\text{tot}}$  (see Eq. 25), dropping picks with  $\sin(\arccos(s/r)) < V_{\text{rad}}/V_{\text{tot}}$ , since  $\sin i \geq V_{\text{rad}}/V_{\text{tot}}$ , see Eq. 7. The largest possible velocity is achieved for equal distances  $D = D_1 = D_2$  and minimal separations  $r_{\text{min}} = s = D\theta$ . This sets the maximum allowed distance to:

$$D_{\text{max}} = \frac{2GM}{\theta V_{\text{tot}}^2}. \quad (27)$$

For a given  $V_{\text{tot}}$  and  $s$ , large values of  $r$  decrease  $s/r$  (increasing the minimal allowed inclination), require smaller values of  $r/a$  (pushing the phase towards pericenter), and/or larger values of eccentricity (see Eq. 3).

We compute a combined distance figure of merit  $\chi_D^2 = \chi_{D_1}^2 + \chi_{D_2}^2$ , where

$$\chi_{D_1}^2 = \frac{(D_1 - \bar{D}_1)^2}{\delta D_1^2}, \chi_{D_2}^2 = \frac{(D_2 - \bar{D}_2)^2}{\delta D_2^2}; \quad (28)$$

and consider the separations ranked by  $\chi_D^2$ . We note that for the set of distances fulfilling this constraint and  $v_{\text{max}} \geq V$  the resulting differences of  $V_{\text{tot}}$  are less than  $10 \text{ m s}^{-1}$  for the two branches of solutions  $D_1 < D_2$  and vice-versa. In contrast, the allowed variations in  $r$  are of the order of 50%, the ones in  $s$  a factor 10 less. The resulting allowed ratios  $s/r$  set the minimal allowed inclinations  $i_{\text{min}} = \arccos(s/r)$ . We sample the full range of allowed inclinations  $i_{\text{min}} \leq i \leq \pi/2$  with 1 to 3 degrees steps and determine the corresponding four allowed  $\phi$  values using Eq. 6. The ratios  $V_{\text{tot}}/v_{\text{max}}$  deliver the values  $r/a = 2 - (V_{\text{tot}}/v_N)^2$  (see Eq. 3) that reproduce the measured total velocity exactly and in turn are linked to the  $s/r$  ratios. From these  $r/a$  values we derive the minimum allowed eccentricity  $e_{\text{min}} = |r/a - 1|$  (see Eq. 2). We sample the range of allowed eccentricities  $e_{\text{min}} \leq e \leq 0.99$  in 0.01 steps and compute the corresponding allowed values of  $\cos(\phi - \phi_0)$  through Eq. 1, each of which delivers two values for

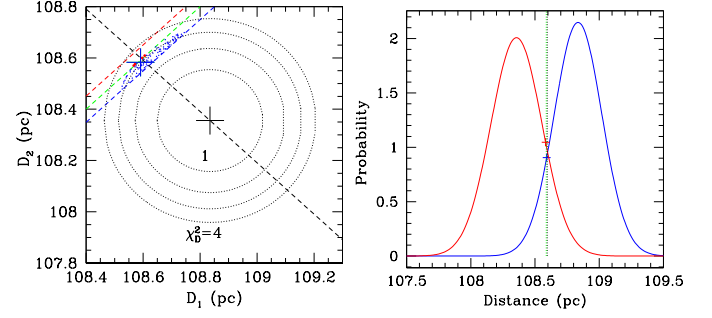


**Fig. 4.** Distances of the binary HD4552,BD+120090. Left: the  $\chi_D^2 = 1, 2, 3, 4$  contours (dotted lines) in the  $D_1, D_2$  plane. The black and blue crosses show the Gaia and best-fitting distances, respectively. The dashed black line shows  $D_{\text{mean}} = \bar{D}_{\text{mean}}$ , the green line shows  $D_1 = D_2$ . The blue and red dashed lines show distances delivering  $r = 2GM/V_{\text{tot}}^2$ . The blue and red dots show the first 100  $D_1$  and  $D_2$  distances (ranked by  $\chi_D^2$ ) with  $v_{\text{max}}/V_{\text{tot}} \leq 1$ . Right: the probability distributions of the distances of HD4552 (blue) and BD+120090 (red). The crosses show the best-fitting Newtonian solution. The dotted black and green lines show  $\bar{D}_{\text{mean}} = (\bar{D}_1 + \bar{D}_2)/2$  and  $D_{\text{mean}} = (D_1 + D_2)/2$ , respectively.

$\phi - \phi_0$ . For each of the allowed values of  $(i, \phi, e, \phi_0)$  we compute  $v_{\text{rad}}/v$  (see Eq. 7) and  $\gamma_{2D}$  (see Eq. 10) and the quantities:

$$\chi_R^2 = \frac{(R - \sin \psi \sin i)^2}{\delta R^2}; \chi_{\Gamma_{2D}}^2 = \frac{(\Gamma_{2D} - \gamma_{2D})^2}{\delta \Gamma_{2D}^2}. \quad (29)$$

We sort the  $\chi^2$  quantity:

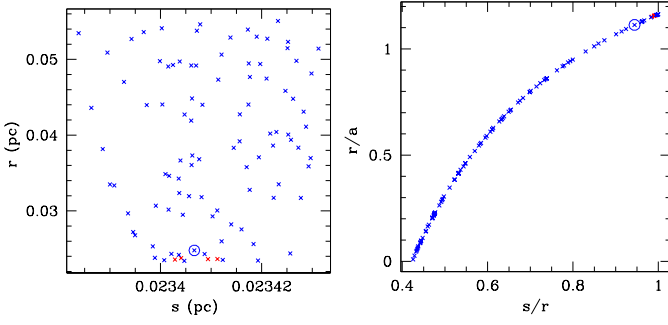
$$\chi^2 = \chi_R^2 + \chi_{\Gamma_{2D}}^2 \quad (30)$$

and we rank the values of  $(i, \phi, e, \phi_0)$  according to  $\chi^2$ . Finally, we select the solutions that reproduce  $\Gamma_{3D}$  best.

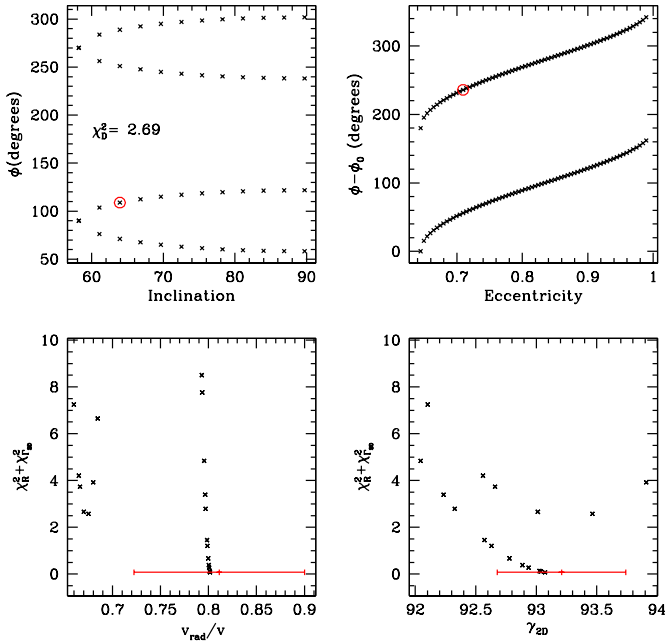
We show an example of the minimization algorithm for the binary HD4552,BD+120090. Figure 4, left, presents the distribution of the best 100 distances with  $v_{\text{max}}/V_{\text{tot}} \leq 1$  ranked by  $\chi_D^2$  for the binary #1, HD4552,BD+120090 in the  $D_1, D_2$  plane. The allowed range of distances is narrow and translates into small ( $\approx 2 \text{ m s}^{-1}$ ) variations of  $V_{\text{ra}}, V_{\text{dec}},$  and  $V_{\text{tan}}$ . The right plot shows the probabilities of the resulting best-fitting distances in 1D. The best fitting solution has distances very near the average distance of the pair and is bracket by the loci of the maximum separation  $r = 2GM/V_{\text{tot}}^2$  allowed by the measured total WB velocity difference. Figure 5, left, shows that the separation  $r$  of the binary is up to a factor 3 larger than the separation  $s$  on the sky. The right plots shows that the value of  $r/a$  needed to reproduce the observed value of  $V_{\text{tot}}$  correlates with  $s/r$ . In turn, the best fitting values of  $s/r$  and  $r/a$  set the minimal allowed inclination and eccentricity (see Eqs. 5 and 2).

Figure 6 illustrates how the orbit parameters  $i, \phi, e, \phi_0$  are constrained for each pair of distances selected in Fig. 5. The inclination is sampled starting from the minimal value set by  $s/r$  and delivers four possible values for  $\phi$  (top left). The eccentricity is sampled starting from the minimal value set by  $r/a$  and delivers two values for  $\phi - \phi_0$  (top right). Each combination of  $i, \phi$  and  $e, \phi - \phi_0$  is considered to achieve  $R = v_{\text{rad}}/v$  (bottom left) and  $\Gamma_{2D} = \gamma_{2D}$  (bottom right) within the errors. The values of  $i, \phi, e, \phi - \phi_0$  that deliver the first or, as in this case, second best of  $\chi^2 = \chi_R^2 + \chi_{\Gamma_{2D}}^2$  and provide the value of  $\gamma_{3D}$  nearest to  $\Gamma_{3D}$  describe the best orbit reproducing the observations. In principle, Eq. 13 allows a direct determination of  $\phi - \phi_0$  as a function of  $e$  for a measured value of  $\Gamma_{3D}$ . However, the larger observational errors affecting  $\Gamma_{3D}$  make the focus on  $\Gamma_{2D}$  preferable. In





**Fig. 5.** Projected and intrinsic separations of the binary HD4552,BD+120090. Left: the distribution of projected and intrinsic separations  $s$  and  $r$ . Right:  $r/a$  as a function of  $s/r$ . Red and blue crosses show  $D_2 \geq D_1$  and  $D_2 < D_1$ , respectively. The circled crosses show the best fitting solution.



**Fig. 6.** The best-fitting Newtonian orbital solution for the binary HD4552,BD+120090. Top left: the angle  $\phi$  as a function of inclination. The red circle shows the selected value. Top right: the angle  $\phi - \phi_0$  as a function of eccentricity. The red circle shows the selected value. Bottom left: the black crosses show  $\chi^2_R + \chi^2_{\gamma_{2D}}$  as a function of  $v_{\text{rad}}/v = \sin \psi \sin i$ . The red cross shows the observed value of  $V_{\text{rad}}/V_{\text{tot}}$  and its error (see Table B.4). Bottom right: the black crosses show  $\chi^2_R + \chi^2_{\gamma_{2D}}$  as a function of  $\gamma_{2D}$ . The red cross shows the value of  $\gamma_{2D}$  and its error (see Table B.4).

the end, the pair of distances  $D_1$  and  $D_2$  that deliver the optimal orbit have a  $\chi^2_D$  value slightly larger (2.7) than the minimal one (2.5). Allowing a 2-3% increase in the total mass of the system is enough to decrease  $\chi^2_D$  to less than 2.

We list the values of the best-fitting solutions in the Tables B.3, B.4, and B.5. The names of the binary pairs are listed in Table B.3. Together with their angular separation, the fitted distances  $D_1$  and  $D_2$ , and  $\chi^2_D$ . Velocities  $V_{\text{ra}}$ ,  $V_{\text{dec}}$ ,  $V_{\text{rad}}$ ,  $V_{\text{tan}}$ ,  $V_{\text{tot}}$  and angles  $\Gamma_{2D}$  and  $\Gamma_{3D}$  are given in Table B.4. The best-fitting quantities  $s$ ,  $r$ ,  $a$ ,  $e_{\text{min}}$ ,  $e$ ,  $i_{\text{min}}$ ,  $i$ ,  $\phi - \phi_0$ ,  $\phi_0$ ,  $\psi$ ,  $\gamma_{2D}$ ,  $\gamma_{3D}$  are listed in Table B.5, together with the period and acceleration of the orbit. These solutions are by no means unique: WBs with low values of  $\chi^2_D$  (roughly one third of the sample) can be fit with different combinations of distances. Given the relatively small size of

our current sample, it goes beyond the scope of the paper to explore which (possibly non-Newtonian) solutions are also viable in these cases.

For the binary #24, HD189739+HD189760, we cannot find any distance for which  $v_{\text{max}} \geq V_{\text{tot}}$ . We report a solution obtained by increasing the total mass of the binary by 33%. Binary #24 not only requires this unrealistically large increase in mass, it also can be fit only by eccentricities almost equal to 1 and orbital periods as large as the age of the universe. We suspect that the system is not bound. The binary is marked in red in the following plots.

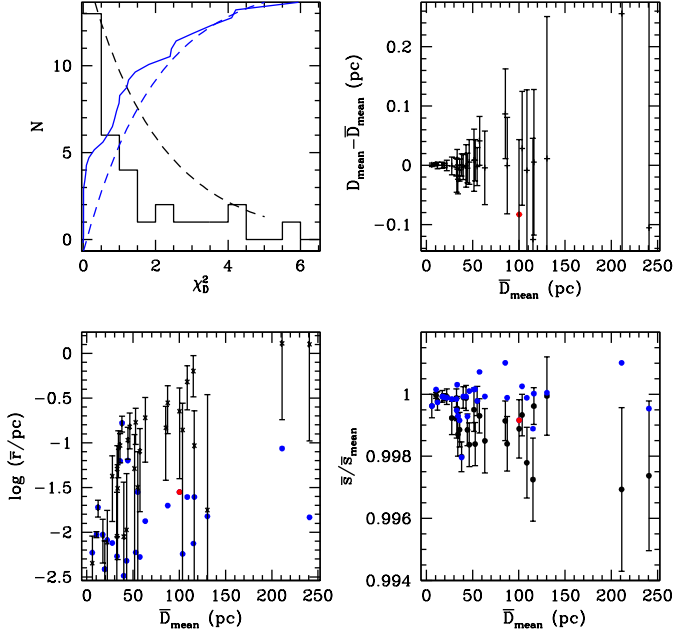
## 5. Results

Figure 7 (top left) shows the histogram of  $\chi^2_D$ . Only seven pairs have  $\chi^2_D > 2$  and the distribution is more peaked at low  $\chi^2_D$  values than the  $\chi^2$  distribution with 2 degrees of freedoms. There are no obvious correlations between  $\chi^2_D$  and  $r$ ,  $s/r$  and  $r/a$ . The top right plot shows that our mean distances  $D_{\text{mean}}$  agree within the errors with the Gaia mean distances. The bottom left plot shows that separations  $\bar{r}$  directly inferred from Gaia distances increase with distance and overestimate the separations  $r$  derived by fitting the measured velocities by more than an order of magnitude. The bottom right plot shows that the WB separation projected on the sky, estimated by scaling the angular separation  $\theta$  with the mean Gaia distance, increasingly overestimates  $\bar{s}$  (obtained by scaling  $\theta$  with the minimal Gaia distance), as the mean distance to the WB increases. Together with the trend of increasing  $\bar{r}$  with  $D_{\text{mean}}$  and the large  $\bar{r}/r$  ratio, this suggests that, dynamical studies of WBs samples with similar distance distributions and using deprojected  $\bar{s}_{\text{mean}}$  run the risk of systematically overestimating the true WB projected separation, therefore underestimating the acceleration and velocity of the system. This, in turn, could bias low the inferred accelerations and mimic a low-acceleration gravitational anomaly. The ratio  $s/\bar{s}_{\text{mean}}$  calculated with our best fitting distances is approximately equal to 1 up to the largest distances and separations.

Figure 8 shows the velocities  $V_{\text{ra}}$ ,  $V_{\text{dec}}$ ,  $V_{\text{rad}}$  and  $V_{\text{tot}}$  as a function of the mean distance of the pair. Our current WB sample is clearly biased against large velocities at large distances. We compare our velocity differences  $V_{\text{tan}}$  and  $V_{\text{tot}}$  to the velocities differences  $\bar{V}_{\text{tan,mean}}$  and  $\bar{V}_{\text{tot,mean}}$  computed using mean Gaia distances in Fig.9 (blue and red points), finding residuals less than  $40 \text{ m s}^{-1}$  and no systematic trends with distances. Differences between  $\bar{V}_{\text{tan}}$  and  $\bar{V}_{\text{tot}}$  (computed scaling the proper motions with the Gaia distances of each star separately) and  $\bar{V}_{\text{tan,mean}}$  and  $\bar{V}_{\text{tot,mean}}$  are much larger, up to  $200 \text{ m s}^{-1}$ , reflecting the uncertainties on the Gaia distances; still, no systematic trends with distances are observed.

The next two figures assess the quality of our best fit solutions. Fig. 10 shows that the ratio  $V_{\text{rad}}/V_{\text{tot}}$ , the angle  $\Gamma_{2D}$  and the angle  $\Gamma_{3D}$  are well reproduced within the errors. The residuals do not show trends with acceleration or separation  $r$ . Fig. 11 presents the same information in terms of velocity residuals, where we have added in quadrature an error equal to 3% of the model values to take into account the uncertainties on the total mass of the binaries. Without WB #24, radial, tangential and parallel velocities are reproduced with RMS of 21, 12 and  $7 \text{ m s}^{-1}$ , respectively. Total velocities are reproduced exactly by construction. This investigation demonstrates that Newtonian solutions can be found down to the lowest accelerations probed by our (small) sample of WBs. Furthermore, Fig. 12 shows the histogram of the ratio  $\tilde{V} = V_{\text{tot}}/V_{\text{circ,s}}$ , where  $V_{\text{circ,s}} = (GM/s)^{1/2}$





**Fig. 7.** The distances and separations of the WB sample. Top left: the histogram of  $\chi^2_D$  values (black full line). The blue line shows the cumulative distribution of  $\chi^2_D$ , the dashed black and blue lines show the  $\chi^2$  distribution and its cumulative for 2 degrees of freedom. Top right: the difference  $D_{\text{mean}} - \bar{D}_{\text{mean}}$  as a function of  $\bar{D}_{\text{mean}}$ . The difference is zero within the errors. Bottom left: crosses show  $\bar{r}$  (the WB separations estimated using Gaia distances and Eq. 15) as a function of the mean WB distance  $\bar{D}_{\text{mean}}$ . The blue and red points show  $r$ , the best fitting WB separations. The largest  $\bar{r}$  are observed at the largest distances. They overestimate  $r$  by an order of magnitude or more. Bottom right: the ratio  $\bar{s}/\bar{s}_{\text{mean}}$  as a function of  $\bar{D}_{\text{mean}}$ . The blue and red points show  $s/\bar{s}_{\text{mean}}$ . The WB separation on the sky  $\bar{s}_{\text{mean}}$  (estimated by scaling the angular separation  $\theta$  with the mean WB distance), increasingly overestimates  $\bar{s}$  (obtained by scaling  $\theta$  with the minimal Gaia distance), as the distance to the WB increases. The best fitting distances deliver  $s/\bar{s}_{\text{mean}} \approx 1$ .

is the Newtonian circular velocity for the current projected separation. As expected, all WBs except binary #24 have  $\tilde{v} < \sqrt{2}$  and in qualitatively agreement with the Newtonian distributions of Pittordis & Sutherland (2018).

In the following we discuss how plausible these (non-unique) solutions are.

The circled WBs in Fig. 10 show that some of the large separation, low-acceleration WBs have inclinations larger than  $70^\circ$ , or eccentricities larger than 0.8, or separations smaller than half the semi-major axis, or phases within  $30^\circ$  of the pericenter. A larger sample of WBs at large separations is needed to assess whether these possibly extreme properties persist.

Figure 13 shows the histograms of best-fitting eccentricities, inclination, phase angles  $\phi - \phi_0$ , and semi-major orientation angles  $\phi_0$ . The eccentricity distribution is approximately thermal ( $f(e)de = 2ede$ ), as expected for WB with separations larger than 1 kAU (Tokovinin 2020). The inclination distribution is peaked towards higher values, to some extent exceeding the expectations from a random distribution of inclinations (flat in  $\cos i$ ). Instead of the expected  $15 \pm 4$  WBs with inclinations larger than  $60^\circ$ , we count  $21 \pm 4$  such systems, possibly still within the range allowed by low-number statistics. The phase distribution has the expected peak at apocenter and a suspicious second peak at pericenter exceeding expectations, but again with

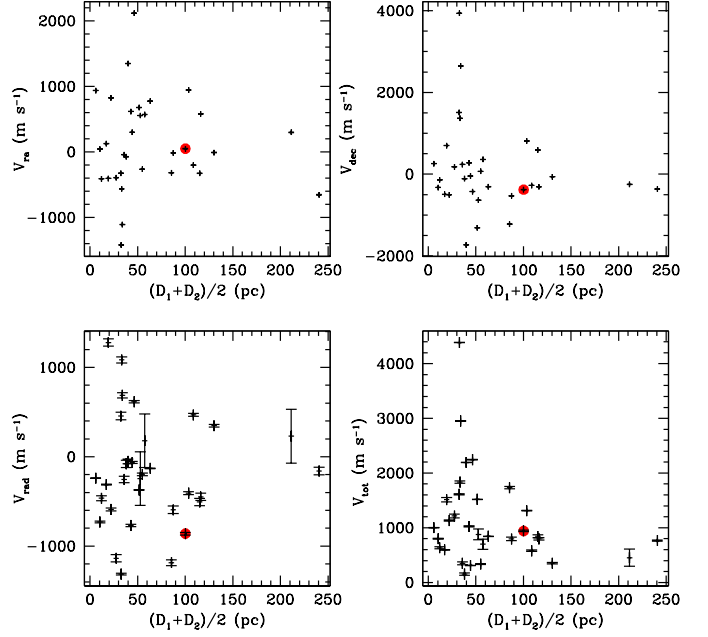


**Fig. 8.** The velocity differences of the WBs. As a function of the mean distance of the pair we show  $V_{\text{ra}}$  (top left),  $V_{\text{dec}}$  (top right),  $V_{\text{rad}}$  (bottom left) and  $V_{\text{tot}}$  (bottom right).

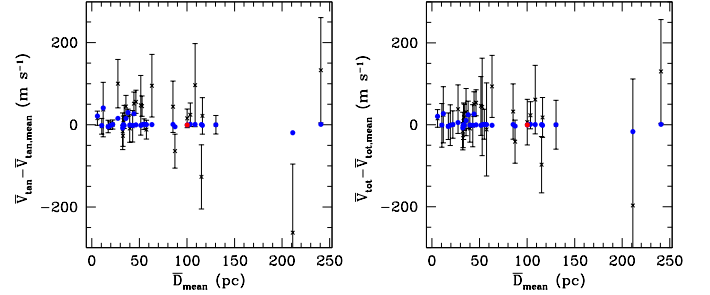
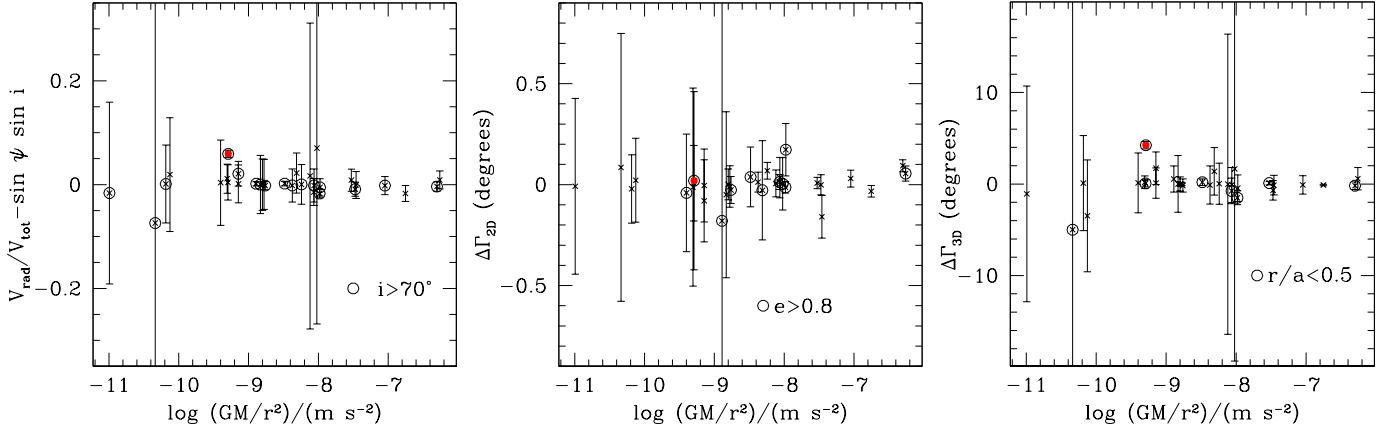


**Fig. 9.** The influence of velocity distance scaling. The blue and red points show the differences between the best fitting  $V_{\text{tan}}$  (left) and  $V_{\text{tot}}$  (right) and  $\bar{V}_{\text{tan,mean}}$  and  $\bar{V}_{\text{tot,mean}}$  (computed by scaling the proper motions with the mean Gaia distances  $\bar{D}_{\text{mean}}$ ) as a function of  $\bar{D}_{\text{mean}}$ . The crosses show the differences between  $\bar{V}_{\text{tan}}$  and  $\bar{V}_{\text{tot}}$  (computed by scaling the proper motions with the Gaia distances of each star separately) and  $\bar{V}_{\text{tan,mean}}$  and  $\bar{V}_{\text{tot,mean}}$ . No systematic trends with distances are observed.

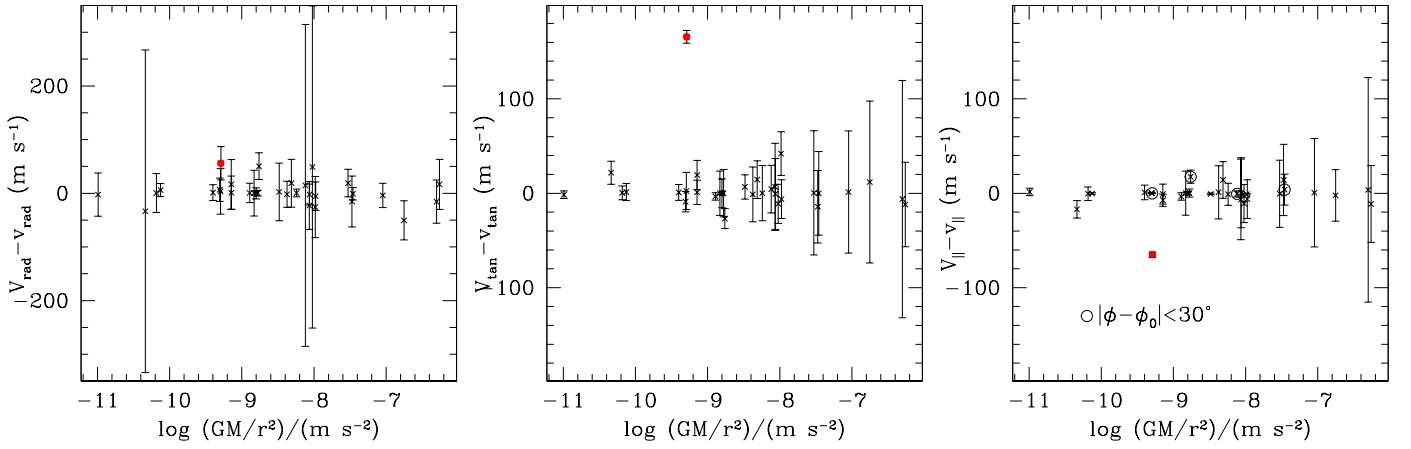
low number statistics. We compute the distribution of expected phases using Eq. 4, averaging over the best-fitting eccentricities. The orientation of the semi-major axis is approximately random, as expected.

Figure 14 shows how the ratios  $s/r$ ,  $V_{\text{rad}}/V_{\text{tot}}$  and  $r/a$  constrain the inclination and eccentricity of the binaries. Two of the high eccentricity WBs are forced to have high inclinations ( $\geq 70^\circ$ ) by the required low values of  $s/r$ , further two by the large  $V_{\text{rad}}/V_{\text{tot}}$  ratio. WBs requiring low or high values of  $r/a$  are forced to have high eccentricities. Five of them have high inclinations, of which one is the possibly unbound pair #24. The measured angle  $\Gamma_{3D}$  forces eight WBs to have large eccentricities ( $\geq 0.8$ ), of which four have high inclination. Four of the WBs with phases near pericenter within  $30^\circ$  have the minimum inclination allowed by the  $V_{\text{rad}}/V_{\text{tot}}$  ratio.

Figure 15 investigates the role of the angle  $\psi$  to reproduce the ratio between the radial and tangential velocities (see Eq.



**Fig. 10.** The residuals  $\Delta V_{\text{rad}}/V_{\text{tot}}$  (left),  $\Delta \Gamma_{2D}$  (middle), and  $\Delta \Gamma_{3D}$  (right) as a function of acceleration. We circle WBs with inclinations larger than  $70^\circ$  in the left, WBs with eccentricities larger than 0.8 in the middle, and WBs with  $r/a < 0.5$  in the right plot.



**Fig. 11.** The residuals  $V_{\text{rad}} - v_{\text{rad}}$  (left),  $V_{\text{tan}} - v_{\text{tan}}$  (middle), and  $V_{\parallel} - v_{\parallel}$  (right) as a function of acceleration.

9). The top panels show, as expected, that the ratio  $|V_{\text{rad}}|/V_{\text{tan}}$  is small for small eccentricities and inclinations and on average larger for large inclinations, with the largest values having also large eccentricities. The bottom panels show that low values of  $|V_{\text{rad}}|/V_{\text{tan}}$  at high eccentricities and inclinations are due to low values of  $|\psi|$ .

Figure 16 show correlations with  $\Gamma_{2D}$  and  $\Gamma_{3D}$ . As expected, both angles are  $\approx 90$  degrees at lowish inclinations and eccentricities. Consistently, the sky position and velocity vectors tend to be parallel or anti-parallel at high inclinations and high eccentricities. While no obvious trend between  $\Gamma_{2D}$  with  $\phi - \phi_0$  appears (bottom left of Fig. 16), the expected modulation (see Eq. 13) of  $\Gamma_{3D}$  with  $\phi - \phi_0$ , scaled by the eccentricity value is clearly seen in the bottom right plot.

Finally, we summarize further (absence of) trends with eccentricities, inclinations, orbital phases, semi-major position angles and separations. There is a lack of eccentricities larger than 0.6 with inclinations lower than 45 degrees. There is a lack of low eccentricities at large separations, and a lack of high eccentricities at smaller separations, in line with the tendency discussed by El-Badry et al. (2021) of WBs having larger  $e$  at larger separations. There are no obvious correlations between eccentricity or inclination and phase  $\phi - \phi_0$  or semi-major axis position  $\phi$ .

## 6. Conclusions

In this work we have introduced two main novelties: the use of accurate radial velocities and the exploitation of the distance distribution provided by the Gaia parallaxes. With these, we are able to constrain the orbits of the WBs to test Einstein-Newton gravity in the low potential regime. We searched for archival data of WB candidates observed with the high precision spectrograph HARPS, finding 44 systems.

Precise RVs, repeated in time, allow to single out and remove multiple systems, and high resolution observations deliver precise chemical abundances and stellar parameters. After cleaning, 32 out of the initial 44 systems (73%) survive our conservative selection criteria and these systems are suitable for testing Einstein-Newton law. The final sample has a median RUWE of 0.975 (with a highest value of 1.24) and a RV median variability of  $10 \pm 6 \text{ m s}^{-1}$ . The star with the highest RV variability ( $29 \text{ m s}^{-1}$ ), is known to host a massive exoplanet.

We obtain for each star an accurate RV, correcting the precise HARPS shifts for gravitational redshift and for convective motions in the stellar atmospheres using 3D model atmospheres. The corrected velocities are accurate to better than  $40 \text{ m s}^{-1}$ . The comparison with Gaia shows a remarkable agreement in the RV zero point ( $67 \text{ m s}^{-1}$ ) with a spread of  $311 \text{ m s}^{-1}$ .

We exploit the distance distributions provided by the Gaia parallaxes to probe projected and tri-dimensional separations

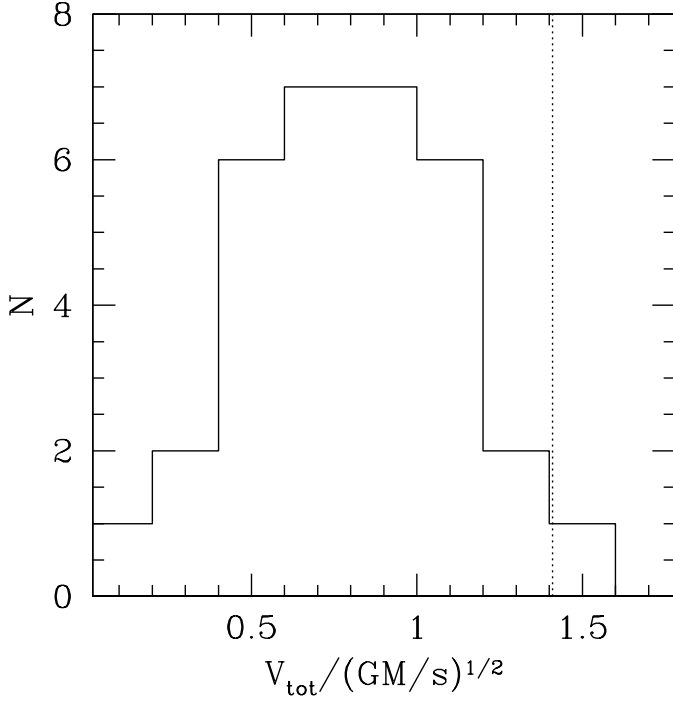


**Fig. 12.** The histogram of the ratio  $\tilde{V} = V_{\text{tot}}/V_{\text{circ},s}$ ; except for WB #24,  $\tilde{V}$  is always less than  $\sqrt{2}$  (dotted vertical line), as expected in Newtonian dynamics.

and velocity differences. In 31 of the 32 WBs at least one Newtonian orbit solution is possible with distances compatible with the Gaia parallax errors, the precision of the total mass estimates and the small velocity errors. For these 31 WBs we obtain reasonable orbit parameters, with some systems possibly too near pericenter and/or at too high inclination. We suspect that the remaining WB, #24, is not bound.

Chae (2024, 2025) finds a remarkable difference between WBs with separations larger than  $\sim 2$  kAU (0.01 pc), and the closer systems, with the widely separated WBs breaking Newton law. We do not detect such a trend with our WB sample, much smaller in size but with higher precision radial velocities. To check whether this conclusion is statistically robust, we are in the process of collecting similarly good RVs for a large sample of WBs, to not only confirm the existence of Newtonian solutions in all cases, but also to verify the distributions of the retrieved orbital parameters are physically acceptable.

**Acknowledgements.** We thank the referee Charalambos Pittordis for a constructive report that helped us improving the presentation of our results. MTM acknowledges the support of the Australian Research Council through Future Fellowship grant FT180100194. Research activities of the Board of Observational and Instrumental Astronomy (NAOS), at the Federal University of Rio Grande do Norte, are supported by continuous grants from the Brazilian funding agency Conselho Nacional de Desenvolvimento Científico (CNPq). I.C.L. (grant No. 313103/2022-4), and J.R.M. (grant No. 308928/2019-9) acknowledge CNPq research fellowships. This work has made use of data from the European Space Agency (ESA) mission *Gaia* (<https://www.cosmos.esa.int/gaia>), processed by the *Gaia* Data Processing and Analysis Consortium (DPAC, <https://www.cosmos.esa.int/web/gaia/dpac/consortium>). Funding for the DPAC has been provided by national institutions, in particular the institutions participating in the *Gaia* Multilateral Agreement.

## References

Banik, I., Pittordis, C., Sutherland, W., et al. 2024, MNRAS, 527, 4573

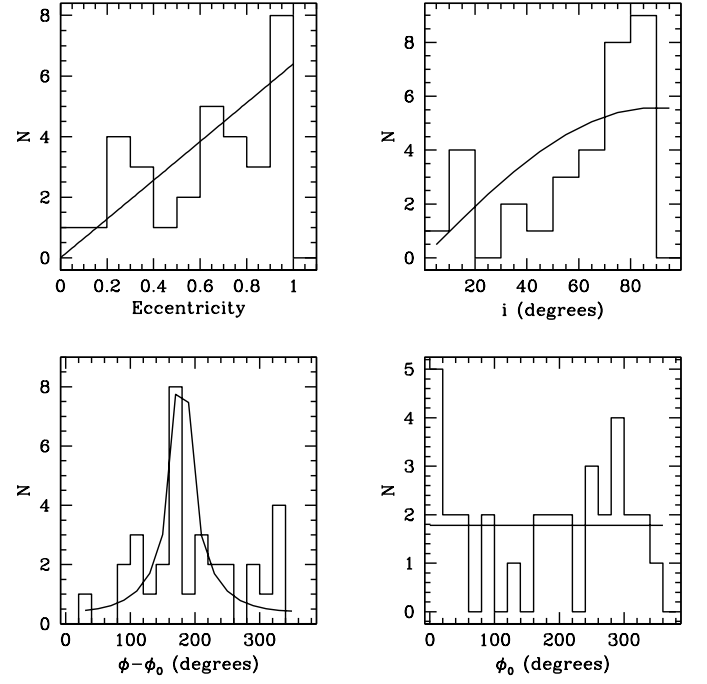


**Fig. 13.** The distributions of best-fitting parameters. The histogram of best-fitting of eccentricities (top left), of inclinations (top right), of phases  $\phi - \phi_0$  (bottom left) and of orientation angles  $\phi_0$  (bottom right) with the expected distributions (black lines).

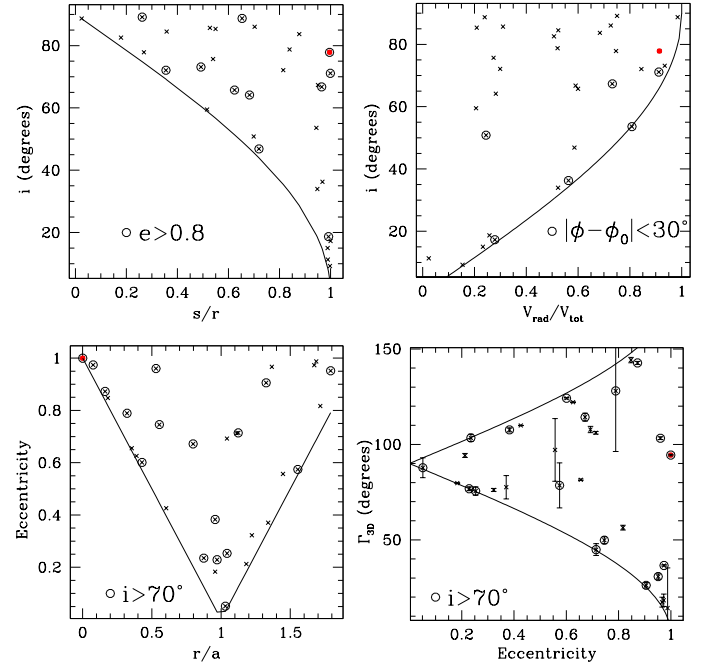


**Fig. 14.** Top left: inclination as a function of  $s/r$ . The line shows the minimum allowed inclination. The circled WBs have eccentricities larger than 0.8. Top right: inclination as a function of  $V_{\text{rad}}/V_{\text{tot}}$ . The line shows the minimum allowed inclination. The circled WBs have phases near the pericenter within  $30^\circ$ . Bottom left: eccentricity as function of  $r/a$ . The line shows the minimum allowed eccentricity. The circled WBs have inclinations larger than  $70^\circ$ . Bottom right:  $\Gamma_{3D}$  as a function of eccentricity. The lines show the allowed angle range. The circled WBs have inclinations larger than  $70^\circ$ .

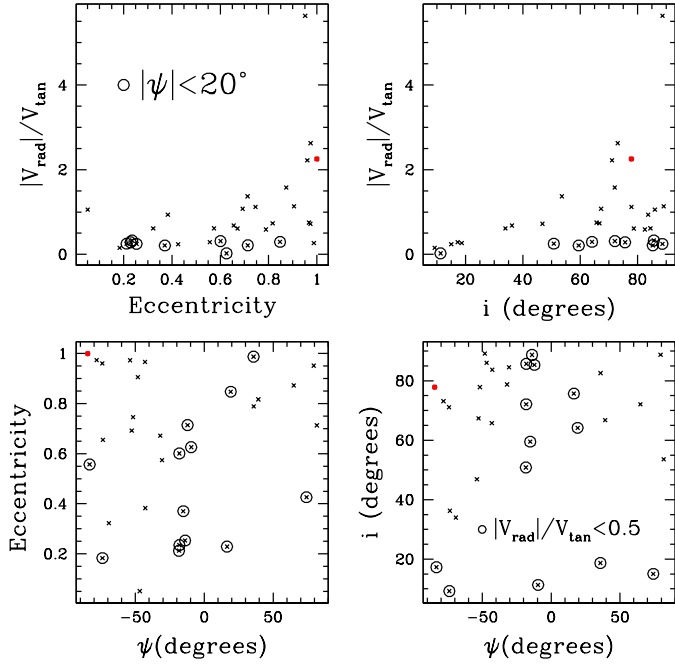


**Fig. 15.** Correlations with  $|V_{\text{rad}}|/V_{\text{tan}}$  (top) and  $|\psi|$  (bottom): eccentricity (left panels) and inclination (right panels). Circled crosses in the top panels show binaries with  $|\psi| < 20^\circ$ ; circled crosses in the bottom panels show binaries with  $|V_{\text{rad}}|/V_{\text{tan}} < 0.5$ .

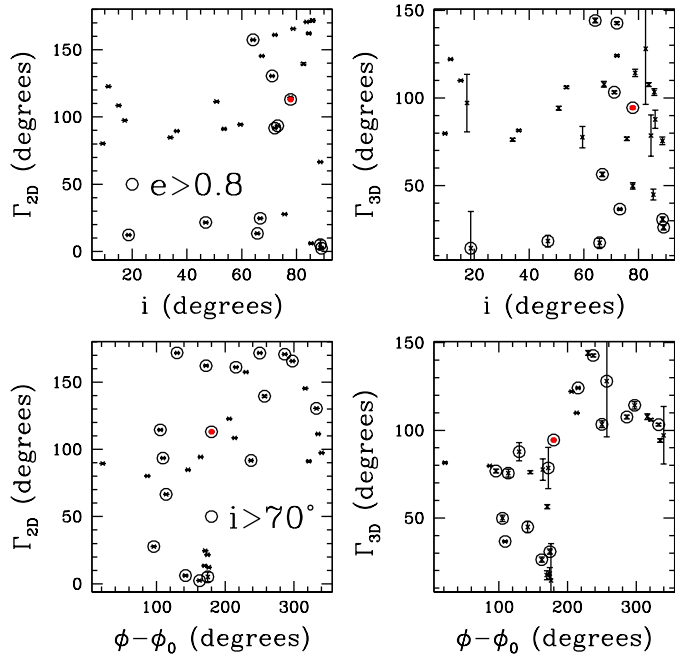


**Fig. 16.** Correlations with  $\Gamma_{2D}$  (left) and  $\Gamma_{3D}$  (right). The top plots show both angles as a function of inclination, circled WBs have eccentricities larger than 0.8. The bottom plots show both angles as function of orbit phase, circled WBs have inclinations larger than  $70^\circ$ .

- Clarke, C. J. 2020, MNRAS, 491, L72  
da Silva, L., Girardi, L., Pasquini, L., et al. 2006, A&A, 458, 609  
El-Badry, K., Rix, H.-W., & Heintz, T. M. 2021, MNRAS, 506, 2269  
Haywood, R. D., Collier Cameron, A., Unruh, Y. C., et al. 2016, MNRAS, 457, 3637  
Hernandez, X., Chae, K.-H., & Aguayo-Ortiz, A. 2024, MNRAS, 533, 729  
Hernandez, X., Cookson, S., & Cortés, R. A. M. 2022, MNRAS, 509, 2304  
Hernandez, X., Jiménez, M. A., & Allen, C. 2012, in Journal of Physics Conference Series, Vol. 405, Journal of Physics Conference Series (IOP), 012018  
Hwang, H.-C., Ting, Y.-S., & Zakamska, N. L. 2022, MNRAS, 512, 3383  
Jiang, Y.-F. & Tremaine, S. 2010, MNRAS, 401, 977  
Katz, D., Sartoretti, P., Guerrier, A., et al. 2023, A&A, 674, A5  
Kervella, P., Arenou, F., & Thévenin, F. 2022, A&A, 657, A7  
Kervella, P., Thévenin, F., & Lovis, C. 2017, A&A, 598, L7  
Lanza, A. F., Molaro, P., Monaco, L., & Haywood, R. D. 2016, A&A, 587, A103  
Leão, I. C., Pasquini, L., Ludwig, H.-G., & de Medeiros, J. R. 2019, MNRAS, 483, 5026  
Lindegren, L., Hernández, J., Bombrun, A., et al. 2018, A&A, 616, A2  
Lo Curto, G., Pepe, F., Avila, G., et al. 2015, The Messenger, 162, 9  
Ludwig, H. G., Caffau, E., Steffen, M., et al. 2009, Mem. Soc. Astron. Italiana, 80, 711  
Mayor, M., Pepe, F., Queloz, D., et al. 2003, The Messenger, 114, 20  
Moutou, C., Mayor, M., Bouchy, F., et al. 2005, A&A, 439, 367  
Pace, G. & Pasquini, L. 2004, A&A, 426, 1021  
Penoyre, Z., Belokurov, V., & Evans, N. W. 2022a, MNRAS, 513, 2437  
Penoyre, Z., Belokurov, V., & Evans, N. W. 2022b, MNRAS, 513, 5270  
Perdelwitz, V., Trifonov, T., Teklu, J. T., Sreenivas, K. R., & Tal-Or, L. 2024, A&A, 683, A125  
Pittordis, C. & Sutherland, W. 2018, MNRAS, 480, 1778  
Pittordis, C. & Sutherland, W. 2019, MNRAS, 488, 4740  
Pittordis, C. & Sutherland, W. 2023, The Open Journal of Astrophysics, 6, 4  
Ramírez, I., Khanal, S., Lichon, S. J., et al. 2019, MNRAS, 490, 2448  
Rodrigues, T. S., Bossini, D., Miglio, A., et al. 2017, MNRAS, 467, 1433  
Rodrigues, T. S., Girardi, L., Miglio, A., et al. 2014, MNRAS, 445, 2758  
Saar, S. H. & Donahue, R. A. 1997, ApJ, 485, 319  
Spina, L., Sharma, P., Meléndez, J., et al. 2021, Nature Astronomy, 5, 1163  
Tokovinin, A. 2020, MNRAS, 496, 987  
Wittrock, J. M., Kane, S. R., Horch, E. P., et al. 2016, AJ, 152, 149

- Barbieri, M. 2024, online; accessed 2024-07-01  
Belokurov, V., Penoyre, Z., Oh, S., et al. 2020, MNRAS, 496, 1922  
Bouchy, F., Pepe, F., & Queloz, D. 2001, A&A, 374, 733  
Bressan, A., Marigo, P., Girardi, L., et al. 2012, MNRAS, 427, 127  
Chae, K.-H. 2023, ApJ, 952, 128  
Chae, K.-H. 2024, ApJ, 960, 114  
Chae, K.-H. 2025, arXiv e-prints, arXiv:2502.09373

## Appendix A: Systems discarded from original sample

Out of the 44 initial systems with HARPS RVs, 12 have been discarded as unsuitable for the present study. We provide the interested reader with the justification of our choice.

HD20430 and HD20439: Our analysis provides an age of  $\sim 700$  Myrs. These stars belong to the Hyades cluster and may just be a proper motion pair.

HD13904 and BD10303B: the last observations in the catalogue of both stars give a difference of  $-0.6 \text{ km s}^{-1}$  with respect to the previous observations. The observations have been re-reduced and the change in radial velocity confirmed. This seems a quadruple system. HD13904 has a RUWE larger than 2.

HD11790: RV varies of  $500 \text{ m s}^{-1}$  in a few days, the star has a companion.

CD-261686 and CD-261686B: there is some confusion amongst the two target in the HARPS observations, and a difference between them of  $3.7 \text{ km s}^{-1}$  in radial velocity, that is in sharp disagreement with the RV difference measured by Gaia for these stars. Such a large RV difference is not compatible with a bound binary and the disagreement with Gaia suggests that the system is multiple.

HIP34407 and HD54100: Spina et al. (2021) report a difference of 0.15 dex in the  $[\text{Fe}/\text{H}]$  of the two stars. Ramírez et al. (2019) notice a spread of  $60 \text{ m s}^{-1}$  in radial velocity in their observations, indicating a possible companion. HARPS spectra (5 and 2 observations respectively) do not show high RV spread.

HD18142 and HD181544: HD 181544 shows a  $30 \text{ m s}^{-1}$  variability on 7 exposures, that is higher than average, and has a RUWE of 1.64.

HD2567 and HD2638: many good HARPS observations are available. HD2638 has a high RV variability ( $47 \text{ m s}^{-1}$ ) but is known to host a Jupiter-planet (Moutou et al. 2005). The system is however triple, with an M star close to HD2638 (Wittrock et al. 2016), so not suitable for the test.

HD169392A and B: HD169392A has a RUWE of 4.2.

HD182817 and HD182797: HD182817 has a RUWE of 1.6 and a RV variability of  $35 \text{ m s}^{-1}$ .

HD116920 and HD116858: HD116920 has a RV variability of  $111 \text{ m s}^{-1}$ .

## Appendix B: Tables

Table B.1. Gaia parameters of the 64 WB stars.

Nr.	Star	$\alpha$ (degrees)	$\delta$ (degrees)	Parallax (mas)	$\text{pm}\alpha$ (mas yr <sup>-1</sup> )	$\text{pm}\delta$ (mas yr <sup>-1</sup> )	RUWE
1	HD4552	11.92189	12.87912	9.188 ± 0.016	84.485 ± 0.021	-35.236 ± 0.016	0.81
1	BD+120090	11.93224	12.87200	9.229 ± 0.017	84.098 ± 0.020	-35.772 ± 0.015	0.90
2	HIP6130	19.67317	-0.86869	36.399 ± 0.025	432.564 ± 0.032	-253.357 ± 0.026	0.91
2	G56.3B	19.66951	-0.87553	36.343 ± 0.031	435.477 ± 0.043	-254.683 ± 0.031	0.88
3	CD-50524	28.10670	-49.53443	8.598 ± 0.013	32.434 ± 0.012	-48.125 ± 0.013	0.99
3	HD11584	28.11510	-49.52397	8.605 ± 0.013	31.377 ± 0.012	-47.560 ± 0.013	1.01
4	HD13357A	32.71752	13.68296	23.304 ± 0.028	114.008 ± 0.032	-72.063 ± 0.027	1.13
4	HD13357B	32.71598	13.68221	23.299 ± 0.027	110.960 ± 0.025	-73.418 ± 0.024	1.06
5	HD20766	49.45525	-62.57243	83.024 ± 0.044	1337.530 ± 0.051	649.840 ± 0.071	0.98
5	HR1010	49.56623	-62.50348	83.061 ± 0.061	1331.027 ± 0.073	647.725 ± 0.083	1.20
6	HD20781	50.01403	-28.78412	27.812 ± 0.024	348.869 ± 0.015	-66.614 ± 0.019	1.04
6	HD20782	50.01667	-28.85436	27.876 ± 0.017	349.054 ± 0.011	-65.305 ± 0.013	0.96
7	HD21209A	50.82325	-49.99072	51.816 ± 0.014	243.931 ± 0.017	270.435 ± 0.016	0.94
7	HD21209B	50.81786	-49.99286	51.825 ± 0.012	239.551 ± 0.014	278.157 ± 0.015	1.05
8	HIP17414	55.96975	16.67062	58.036 ± 0.018	157.855 ± 0.023	-316.199 ± 0.015	1.04
8	HIP17405	55.93925	16.66589	58.028 ± 0.029	156.277 ± 0.036	-310.112 ± 0.025	0.89
9	HD24062	56.19506	-70.02708	18.185 ± 0.014	-10.078 ± 0.018	-97.117 ± 0.017	1.01
9	HD24085	56.25634	-70.02453	18.177 ± 0.016	-9.063 ± 0.019	-97.347 ± 0.018	1.03
10	HD26913	63.85699	6.19915	45.308 ± 0.024	-101.753 ± 0.026	-112.115 ± 0.019	1.05
10	HD26923	63.86951	6.18638	45.300 ± 0.028	-109.614 ± 0.041	-107.279 ± 0.027	1.10
11	HD29167	67.98291	-59.87497	9.665 ± 0.013	-25.045 ± 0.017	-25.669 ± 0.016	1.01
11	HD29167B	67.98571	-59.87407	9.652 ± 0.012	-26.967 ± 0.015	-27.325 ± 0.016	0.94
12	HIP33705	105.04082	-31.14153	26.307 ± 0.017	18.770 ± 0.016	35.760 ± 0.018	0.93
12	HIP33691	105.01155	-31.22792	26.201 ± 0.020	19.094 ± 0.020	36.210 ± 0.019	1.03
13	HIP47836	146.25754	-49.48673	17.400 ± 0.017	-23.567 ± 0.020	97.339 ± 0.017	0.82
13	HIP47839	146.26511	-49.48493	17.425 ± 0.018	-21.476 ± 0.021	98.666 ± 0.018	0.95
14	HD96273	166.53082	7.03319	8.652 ± 0.021	-14.902 ± 0.022	-61.708 ± 0.019	0.92
14	AG+071510	166.53143	7.03095	8.700 ± 0.015	-14.303 ± 0.018	-62.787 ± 0.014	0.82
15	HD104760	180.94350	-44.12272	18.975 ± 0.019	99.110 ± 0.016	18.378 ± 0.014	0.98
15	HD104759	180.94943	-44.11789	18.915 ± 0.016	101.332 ± 0.012	15.840 ± 0.011	0.87
16	HD106515A	183.77623	-7.25755	29.315 ± 0.030	-251.469 ± 0.031	-51.330 ± 0.022	0.97
16	HD106515B	183.77432	-7.25769	29.391 ± 0.029	-244.604 ± 0.031	-67.744 ± 0.021	1.00
17	HD133131A	225.89847	-27.84315	19.433 ± 0.027	156.227 ± 0.035	-133.767 ± 0.038	1.24
17	HD133131B	225.90001	-27.84161	19.413 ± 0.029	159.010 ± 0.035	-139.133 ± 0.037	1.02
18	HD135101A	228.17838	19.28734	30.803 ± 0.021	-595.904 ± 0.022	293.484 ± 0.023	1.01
18	HD135101B	228.17961	19.29370	30.795 ± 0.020	-593.723 ± 0.024	283.636 ± 0.019	1.00
19	HD143336	240.25829	-32.30296	7.670 ± 0.020	-9.847 ± 0.025	-0.293 ± 0.018	1.12
19	HD143336B	240.25702	-32.30713	7.669 ± 0.020	-9.864 ± 0.025	-0.392 ± 0.018	1.08
20	HD147722	246.16608	-29.70388	30.537 ± 0.024	80.106 ± 0.029	-104.506 ± 0.022	1.01
20	HD147723	246.16609	-29.70501	30.489 ± 0.048	70.979 ± 0.065	-79.144 ± 0.046	1.13
21	HD154363	256.26007	-5.07157	95.567 ± 0.024	-916.343 ± 0.025	-1138.762 ± 0.019	0.99
21	GJ654	256.30331	-5.09927	95.560 ± 0.021	-917.207 ± 0.023	-1132.153 ± 0.016	0.90
22	GJ663A	258.83411	-26.60681	168.003 ± 0.134	-498.600 ± 0.123	-1149.158 ± 0.086	0.69
22	36OphB	258.83508	-26.60790	168.130 ± 0.108	-465.861 ± 0.111	-1141.168 ± 0.073	0.67
23	HD177730	286.58783	-10.71872	11.455 ± 0.015	-66.132 ± 0.015	-52.104 ± 0.013	0.88
23	BD-104948B	286.58456	-10.72006	11.419 ± 0.015	-66.080 ± 0.014	-50.817 ± 0.012	0.89
24	HD189739	300.40402	-1.67133	9.961 ± 0.018	-6.810 ± 0.021	-16.025 ± 0.013	1.10
24	HD189760	300.41946	-1.67565	9.984 ± 0.017	-6.914 ± 0.020	-15.227 ± 0.013	0.97
25	CPD-5211628	302.42477	-52.19092	4.165 ± 0.017	17.442 ± 0.019	13.441 ± 0.015	1.20
25	CPD-5211628B	302.42767	-52.19017	4.143 ± 0.020	18.016 ± 0.019	13.758 ± 0.016	1.21
26	HD192343	303.53766	6.57695	15.844 ± 0.024	-129.763 ± 0.026	-59.661 ± 0.019	0.88
26	HD192344	303.54013	6.58872	15.796 ± 0.020	-132.350 ± 0.024	-58.640 ± 0.017	0.90
27	HD196067	310.43649	-75.35153	25.033 ± 0.021	156.404 ± 0.019	-162.214 ± 0.022	1.18
27	HD196068	310.44254	-75.34717	25.038 ± 0.017	163.531 ± 0.016	-171.346 ± 0.018	1.04
28	WASP-94A	313.78323	-34.13576	4.750 ± 0.024	26.500 ± 0.021	-44.971 ± 0.018	0.98
28	WASP-94B	313.78830	-34.13573	4.721 ± 0.016	26.191 ± 0.014	-44.702 ± 0.012	0.81
29	HD201247A	317.60666	-54.57384	30.060 ± 0.021	128.400 ± 0.020	-21.441 ± 0.018	0.89
29	HD201247B	317.60809	-54.57462	30.032 ± 0.021	131.971 ± 0.019	-30.112 ± 0.018	0.96
30	HD201796A	318.09451	-15.00028	21.512 ± 0.025	76.573 ± 0.027	-39.280 ± 0.022	0.85
30	HD201796B	318.09360	-14.99953	21.582 ± 0.025	66.951 ± 0.028	-37.343 ± 0.024	0.94
31	HD206429	325.99500	-57.32549	22.543 ± 0.020	-116.541 ± 0.019	-52.780 ± 0.017	0.96
31	HD206428	326.00061	-57.28329	22.594 ± 0.016	-115.253 ± 0.016	-53.057 ± 0.015	0.94
32	HD221550A	353.33633	-47.30132	11.705 ± 0.015	91.941 ± 0.009	-87.166 ± 0.013	0.92
32	HD221550B	353.33612	-47.30294	11.726 ± 0.014	92.720 ± 0.009	-84.145 ± 0.012	0.94



**Table B.2.** Stellar parameters and radial velocities of the 64 WB stars. The gravity values given in italics are Gaia values.

Nr.	Star	Age (Gyr)	T <sub>eff</sub> (K)	log g (m s <sup>-2</sup> )	[Fe/H] (dex)	Mass (M <sub>⊙</sub> )	Radius (R <sub>⊙</sub> )	GR (km s <sup>-1</sup> )	V <sub>con</sub> (km s <sup>-1</sup> )	Mask/N	RV (km s <sup>-1</sup> )
1	HD4552	2.6	6278 ± 23	4.323 ± 0.056	-0.005 ± 0.016	1.15	1.13	0.65	-0.67	G2/13	14.761 ± 0.005
1	BD+120090	6.3	5994 ± 6	4.298 ± 0.016	-0.011 ± 0.005	1.03	1.18	0.56	-0.59	G2/13	15.219 ± 0.016
2	HIP6130	13.8	5300 ± 50	4.43 ± 0.1	-0.13 ± 0.05	0.8	0.79	0.64	-0.39	K5/11	17.140 ± 0.01
2	G56.3B	5.1	3930 ± 100	<i>4.40</i>	9999 ± 9999	0.55	0.49	0.71	-0.32	K5/2	18.416 ± 0.002
3	CD-50524	1.6	6224 ± 9	4.385 ± 0.029	-0.091 ± 0.007	1.1	1.04	0.67	-0.64	G2/13	22.080 ± 0.002
3	HD11584	2.8	6268 ± 11	4.353 ± 0.026	-0.056 ± 0.008	1.12	1.16	0.61	-0.66	G2/13	22.449 ± 0.003
4	HD13357A	13.6	5638 ± 50	4.33 ± 0.1	-0.08 ± 0.05	0.88	0.97	0.58	-0.48	G2/84	25.209 ± 0.009
4	HD13357B	13.8	5338 ± 50	4.36 ± 0.1	-0.08 ± 0.05	0.85	0.86	0.63	-0.41	G2/3	26.098 ± 0.01
5	HD20766	3.2	5771 ± 23	4.547 ± 0.036	-0.189 ± 0.019	0.92	0.85	0.69	-0.47	G2/65	12.555 ± 0.026
5	HR1010	3.3	5878 ± 5	4.513 ± 0.011	-0.231 ± 0.004	0.93	0.88	0.67	-0.51	G2/405	12.031 ± 0.01
6	HD20781	13.8	5324 ± 52	4.51 ± 0.1	0.04 ± 0.04	0.88	0.82	0.68	-0.38	G2/237	40.368 ± 0.005
6	HD20782	9.1	5789 ± 38	4.41 ± 0.12	-0.02 ± 0.03	0.96	0.92	0.66	-0.51	G2/87	39.964 ± 0.035
7	HD21209A	5	4620 ± 50	4.45 ± 0.2	-0.39 ± 0.05	0.65	0.61	0.68	-0.3	K5/64	-8.935 ± 0.008
7	HD21209B	5.1	3908 ± 100	<i>4.683</i>	9999 ± 9999	0.47	0.41	0.73	-0.32	K5/11	-7.627 ± 0.007
8	HIP17414	13.8	3628 ± 100	<i>4.019</i>	9999 ± 9999	0.52	0.51	0.65	-0.38	K5/2	34.509 ± 0.003
8	HIP17405	6.2	3558 ± 100	<i>4.449</i>	9999 ± 9999	0.48	0.43	0.71	-0.4	M2/3	34.858 ± 0.003
9	HD24062	4.6	6001 ± 5	4.253 ± 0.014	0.215 ± 0.005	1.14	1.32	0.55	-0.6	G2/60	27.590 ± 0.01
9	HD24085	4.4	6039 ± 5	4.298 ± 0.013	0.154 ± 0.004	1.12	1.23	0.58	-0.6	G2/26	27.817 ± 0.009
10	HD26913	4	5741 ± 11	4.502 ± 0.024	-0.029 ± 0.009	0.96	0.9	0.68	-0.47	G2/6	-7.679 ± 0.011
10	HD26923	0.94	6047 ± 9	4.512 ± 0.019	-0.009 ± 0.007	1.07	0.98	0.69	-0.56	G2/60	-7.169 ± 0.013
11	HD29167	3.3	5893 ± 21	4.502 ± 0.047	-0.042 ± 0.016	1	0.94	0.68	-0.52	G2/2	11.505 ± 0.013
11	HD29167B	2.2	5927 ± 29	4.525 ± 0.05	0 ± 0.02	1.03	0.95	0.69	-0.52	G2/2	11.922 ± 0.008
12	HIP33705	2.7	6470 ± 50	<i>4.144</i>	-0.25 ± 0.2	1.15	1.28	0.57	-0.782	G2/2	16.343 ± 0.003
12	HIP33691	3.6	5450 ± 50	<i>4.495</i>	-0.07 ± 0.2	0.88	0.83	0.67	-0.41	G2/2	16.895 ± 0.001
13	HIP47836	5.8	6072 ± 11	4.407 ± 0.03	-0.31 ± 0.01	0.94	0.99	0.6	-0.59	G2/20	-1.977 ± 0.006
13	HIP47839	4.9	6149 ± 12	4.402 ± 0.04	-0.306 ± 0.01	0.98	1.01	0.62	-0.61	GG	-1.797 ± 0.3
14	HD96273	4.7	6403 ± 20	4.228 ± 0.045	-0.348 ± 0.013	1.05	1.29	0.52	-0.74	G2/15	-4.296 ± 0.01
14	AG+071510	4.6	5870 ± 11	4.503 ± 0.024	-0.267 ± 0.008	0.9	0.88	0.65	-0.51	G2/14	-3.430 ± 0.006
15	HD104760	6.1	5900 ± 50	4.32 ± 0.1	0.07 ± 0.05	1.03	1.01	0.65	-0.56	G2/11	6.368 ± 0.005
15	HD104759	12.9	5523 ± 50	4.41 ± 0.1	0.06 ± 0.05	0.9	0.92	0.62	-0.44	GG	6.213 ± 0.3
16	HD106515A	13.8	5364 ± 57	4.39 ± 0.18	0.016 ± 0.009	0.85	0.83	0.65	-0.41	G2/27	20.781 ± 0.029
16	HD106515B	13.8	5190 ± 58	4.3 ± 0.2	0.022 ± 0.01	0.81	0.79	0.65	-0.39	G2/4	20.114 ± 0.002
17	HD133131A	8.3	5819 ± 6	4.458 ± 0.018	-0.272 ± 0.005	0.87	0.9	0.62	-0.5	G2/8	-16.052 ± 0.002
17	HD133131B	8.6	5826 ± 12	4.447 ± 0.035	-0.285 ± 0.01	0.86	0.91	0.6	-0.51	G2/4	-16.454 ± 0.002
18	HD135101A	13	5612 ± 50	4.16 ± 0.1	0.03 ± 0.05	0.91	1.29	0.45	-0.51	G2/69	-38.829 ± 0.013
18	HD135101B	13.8	5444 ± 50	4.4 ± 0.1	0.03 ± 0.05	0.87	0.89	0.62	-0.42	G2/2	-39.024 ± 0.002
19	HD143336	3	6208 ± 22	4.377 ± 0.066	-0.051 ± 0.014	1.1	1.11	0.63	-0.64	G2/3	-19.693 ± 0.011
19	HD143336B	3.9	5943 ± 11	4.472 ± 0.036	-0.118 ± 0.008	0.98	0.94	0.66	-0.54	G2/2	-19.216 ± 0.01
20	HD147722	4.7	6025 ± 5	4.295 ± 0.013	0.125 ± 0.005	1.1	1.2	0.58	-0.6	G2/14	-1.008 ± 0.01
20	HD147723	5.4	6026 ± 9	4.098 ± 0.017	0.139 ± 0.007	1.16	1.59	0.46	-0.64	G2/19	-2.481 ± 0.003
21	HD154363	13.8	4400 ± 100	4.6 ± 0.1	-0.59 ± 0.1	0.57	0.55	0.66	-0.28	K5/71	34.222 ± 0.008
21	GJ654	13.8	3658 ± 70	4.79 ± 0.2	-0.36 ± 0.2	0.52	0.41	0.81	-0.37	M2/195	35.012 ± 0.003
22	GJ663A	13.8	5087 ± 50	4.58 ± 0.1	-0.25 ± 0.05	0.74	0.7	0.67	-0.33	K5/57	0.620 ± 0.001
22	36OphB	13.8	4979 ± 50	4.53 ± 0.1	-0.32 ± 0.05	0.7	0.68	0.66	-0.32	K5/57	0.380 ± 0.001
23	HD177730	0.9	5926 ± 9	4.535 ± 0.017	-0.07 ± 0.006	1.01	0.92	0.7	-0.52	G2/8	2.074 ± 0.008
23	BD-104948B	1	5925 ± 7	4.53 ± 0.014	-0.071 ± 0.005	1.01	0.92	0.7	-0.52	G2/8	2.668 ± 0.012
24	HD189739	4.5	6138 ± 11	4.283 ± 0.027	0.01 ± 0.009	1.1	1.24	0.56	-0.64	G2/16	-60.548 ± 0.004
24	HD189760	4.8	6087 ± 11	4.308 ± 0.029	0.017 ± 0.009	1.08	1.2	0.57	-0.61	G2/16	-59.647 ± 0.014
25	CPD-5211628	4.5	5088 ± 30	3.7 ± 0.068	0.162 ± 0.022	1.29	2.62	0.31	-0.46	G2/1	11.670 ± 0.01
25	CPD-5211628B	11.4	5483 ± 23	4.038 ± 0.046	0.169 ± 0.018	1	1.57	0.41	-0.5	G2/1	11.890 ± 0.01
26	HD192343	7.8	5783 ± 5	4.188 ± 0.011	0.219 ± 0.005	1.05	1.31	0.51	-0.55	G2/14	-0.429 ± 0.002
26	HD192344	8.7	5687 ± 7	4.07 ± 0.015	0.199 ± 0.007	1.06	1.54	0.44	-0.55	G2/14	-0.359 ± 0.003
27	HD196067	4.5	6005 ± 6	4.203 ± 0.015	0.19 ± 0.007	1.12	1.21	0.59	-0.61	G2/36	-10.802 ± 0.016
27	HD196068	4	5975 ± 4	4.298 ± 0.011	0.279 ± 0.004	1.14	1.24	0.58	-0.58	G2/18	-10.834 ± 0.02
28	WASP-94A	2.2	6198 ± 8	4.3 ± 0.02	0.318 ± 0.006	1.25	1.29	0.62	-0.65	G2/65	-8.805 ± 0.016
28	WASP-94B	1.5	6112 ± 6	4.38 ± 0.02	0.305 ± 0.005	1.21	1.16	0.66	-0.61	GG	-8.955 ± 0.3
29	HD201247A	3.6	5742 ± 10	4.512 ± 0.02	-0.007 ± 0.008	0.98	0.91	0.69	-0.47	G2/6	-3.357 ± 0.024
29	HD201247B	4	5632 ± 14	4.533 ± 0.024	0.016 ± 0.01	0.95	0.88	0.69	-0.44	G2/6	-4.410 ± 0.024
30	HD201796A	4.4	5865 ± 9	4.503 ± 0.018	0.122 ± 0.008	1.05	0.99	0.67	-0.51	G2/9	-20.627 ± 0.01
30	HD201796B	2.7	5843 ± 10	4.513 ± 0.018	0.118 ± 0.008	0.96	0.9	0.68	-0.5	G2/6	-21.222 ± 0.008
31	HD206429	5.1	6321 ± 23	4.133 ± 0.043	-0.235 ± 0.015	1.09	1.46	0.48	-0.73	G2/22	37.173 ± 0.002
31	HD206428	4.1	6373 ± 21	4.292 ± 0.049	-0.268 ± 0.014	1.06	1.2	0.56	-0.71	G2/22	37.209 ± 0.012
32	HD221550A	6.4	5634 ± 10	4.49 ± 0.03	-0.018 ± 0.008	0.92	0.89	0.66	-0.45	G2/11	8.306 ± 0.022
32	HD221550B	4.2	5633 ± 14	4.525 ± 0.025	-0.027 ± 0.009	0.93	0.87	0.68	-0.44	G2/8	9.521 ± 0.023

**Table B.3.** Angular separations, masses and recovered distances of the 32 WBs.

Nr.	Star 1	Star 2	$(\alpha_1 - \alpha_2) \cos \delta$ ( $''$ )	$\delta_1 - \delta_2$ ( $''$ )	$\theta$ ( $''$ )	M ( $M_\odot$ )	$D_1$ (pc)	$D_2$ (pc)	$\chi_D^2$
1	HD4552	BD+120090	36.31	-25.65	44.46	2.18	108.591	108.583	3.033
2	HIP6130	G56.3B	13.17	24.60	27.90	1.35	27.490	27.497	1.435
3	CD-50524	HD11584	19.62	37.64	42.45	2.22	116.265	116.271	0.154
4	HD13357A	HD13357B	5.38	2.69	6.02	1.73	42.912	42.917	0.008
5	HD20766	HR1010	184.23	248.21	309.11	1.85	12.045	12.039	0.004
6	HD20781	HD20782	8.35	-252.85	252.99	1.84	35.928	35.884	0.991
7	HD21209A	GJ56.3B	-12.48	-7.71	14.67	1.12	19.299	19.296	0.000
8	HIP17414	HIP17405	105.17	17.04	106.54	1	17.231	17.234	0.002
9	HD24062	HD24085	-75.36	-9.18	75.91	2.26	54.989	55.009	0.009
10	HD26913	HD26923	-44.81	45.98	64.20	2.03	22.070	22.075	0.006
11	HD29167	HD29167B	5.06	3.21	6.00	2.03	103.565	103.569	0.543
12	HIP33705	HIP33691	90.15	311.03	323.83	2.03	38.012	38.168	0.004
13	HIP47836	HIP47839	17.71	6.48	18.86	1.92	57.472	57.471	1.811
14	HD96273	AG+071510	-2.13	8.06	8.34	1.95	115.132	115.138	3.535
15	HD104760	HD104759	-15.37	-17.39	23.21	1.93	52.793	52.793	5.953
16	HD106515A	HD106515B	6.83	0.50	6.85	1.66	34.045	34.045	4.218
17	HD133131A	HD133131B	4.85	5.55	7.37	1.73	51.495	51.494	0.307
18	HD135101A	HD135101B	-4.22	-22.88	23.26	1.78	32.463	32.467	0.067
19	HD143336	HD143336B	3.88	15.03	15.53	2.08	130.397	130.385	0.005
20	HD147722	HD147723	0.06	-4.07	4.07	2.26	32.756	32.756	0.806
21	HD154363	GJ654	-155.15	99.70	184.42	1.09	10.466	10.466	1.006
22	GJ663A	36OphB	3.21	-3.93	5.07	1.44	5.954	5.948	0.086
23	HD177730	BD-104948B	11.61	4.84	12.57	2.02	87.425	87.444	2.563
24	HD189739	HD189760	55.50	-15.54	57.64	2.18	100.193	100.195	1.199
25	CPD-5211628	CPD-5211628B	-6.38	-2.68	6.92	2.29	240.614	240.627	0.679
26	HD192343	HD192344	-8.79	-42.36	43.27	2.11	63.206	63.207	2.435
27	HD196067	HD196068	5.49	15.69	16.62	2.26	39.941	39.941	0.043
28	WASP-94A	WASP-94B	-15.06	-0.10	15.06	2.46	211.396	211.481	0.867
29	HD201247A	HD201247B	-3.08	2.82	4.18	1.93	33.292	33.293	1.247
30	HD201796A	HD201796B	-3.28	2.67	4.23	2.01	46.414	46.416	4.099
31	HD206429	HD206428	10.92	151.89	152.29	2.15	44.332	44.278	0.918
32	HD221550A	HD221550B	-0.48	-5.83	5.85	1.85	85.444	85.445	2.404

**Table B.4.** Measured velocities and angles of the 32 WBs.

Nr.	$V_{ra}$ (m s <sup>-1</sup> )	$V_{dec}$ (m s <sup>-1</sup> )	$V_{rad}$ (m s <sup>-1</sup> )	$V_{tan}$ (m s <sup>-1</sup> )	$V_{tot}$ (m s <sup>-1</sup> )	$\Gamma_{2D}$ (degree)	$\Gamma_{3D}$ (degree)
1	-202.4 ± 3.1	-274.8 ± 2.4	468.0 ± 16.8	341.3 ± 2.8	579.2 ± 13.3	91.1 ± 0.5	106.1 ± 0.7
2	-393.2 ± 1.5	180.7 ± 1.1	-1136.0 ± 41.3	432.7 ± 1.5	1215.6 ± 34.8	93.5 ± 0.1	36.6 ± 0.4
3	581.6 ± 2.0	-309.6 ± 2.1	-449.0 ± 40.2	658.9 ± 2.1	797.3 ± 23.0	89.5 ± 0.2	81.5 ± 0.4
4	617.6 ± 1.7	277.2 ± 1.6	-769.0 ± 13.4	677.0 ± 1.7	1024.5 ± 10.4	2.4 ± 0.1	26.2 ± 1.5
5	-408.4 ± 1.1	-138.8 ± 1.3	-464.0 ± 27.9	431.3 ± 1.1	633.5 ± 19.2	145.4 ± 0.2	107.8 ± 1.7
6	-42.2 ± 0.7	236.8 ± 0.8	-254.0 ± 35.4	240.5 ± 0.8	349.8 ± 24.8	171.8 ± 0.2	87.8 ± 5.2
7	-404.8 ± 0.4	701.7 ± 0.4	1278.0 ± 41.4	810.1 ± 0.4	1513.1 ± 38.4	91.7 ± 0.1	142.7 ± 0.8
8	126.7 ± 0.7	-492.8 ± 0.5	-312.0 ± 4.2	508.9 ± 0.5	596.9 ± 2.4	84.8 ± 0.1	76.1 ± 0.8
9	-263.6 ± 1.4	68.8 ± 1.3	-197.0 ± 13.4	272.5 ± 1.7	336.2 ± 8.9	21.6 ± 0.3	18.4 ± 3.3
10	824.7 ± 1.1	-503.7 ± 0.7	-590.0 ± 17.0	966.4 ± 1.1	1132.2 ± 8.2	165.7 ± 0.1	114.3 ± 2.1
11	944.2 ± 2.4	813.7 ± 2.4	-407.0 ± 15.3	1246.4 ± 2.5	1311.1 ± 5.2	171.7 ± 0.1	103.4 ± 1.9
12	-72.6 ± 1.0	-107.9 ± 1.0	-80.0 ± 40.1	130.1 ± 1.0	152.7 ± 20.0	162.2 ± 0.4	78.5 ± 11.8
13	569.7 ± 1.7	361.3 ± 1.4	180.0 ± 300.1	674.6 ± 1.7	698.2 ± 94.9	12.3 ± 0.1	14.3 ± 21.0
14	-326.6 ± 3.2	590.6 ± 2.7	-506.0 ± 41.7	674.9 ± 2.4	843.5 ± 27.6	13.4 ± 0.2	17.4 ± 2.6
15	556.0 ± 1.1	-635.4 ± 1.0	-245.0 ± 300.0	844.3 ± 1.2	879.1 ± 97.8	97.4 ± 0.1	97.1 ± 16.4
16	-1107.8 ± 1.5	2649.0 ± 1.0	687.0 ± 29.1	2871.3 ± 1.0	2952.4 ± 7.1	108.5 ± 0.1	109.9 ± 0.1
17	677.9 ± 2.5	-1308.6 ± 2.7	-372.0 ± 2.8	1473.7 ± 2.5	1520.0 ± 2.4	111.5 ± 0.1	94.2 ± 1.1
18	-324.5 ± 1.0	1510.3 ± 1.0	455.0 ± 42.1	1544.7 ± 1.0	1610.4 ± 12.4	157.4 ± 0.1	144.2 ± 1.4
19	-10.0 ± 4.6	-60.8 ± 3.3	347.0 ± 14.9	61.6 ± 3.4	352.4 ± 15.0	5.1 ± 3.5	30.8 ± 1.4
20	-1417.4 ± 2.3	3938.5 ± 1.7	-1313.0 ± 10.4	4185.8 ± 1.7	4386.9 ± 3.6	161.1 ± 0.1	124.2 ± 0.4
21	44.5 ± 0.4	-325.9 ± 0.3	-730.0 ± 8.5	328.9 ± 0.3	800.7 ± 7.2	130.5 ± 0.1	103.2 ± 0.7
22	937.1 ± 1.0	257.5 ± 0.7	-240.0 ± 1.4	971.8 ± 1.0	1001.0 ± 1.1	66.5 ± 0.1	75.6 ± 2.2
23	-15.4 ± 1.8	-529.1 ± 1.6	-594.0 ± 42.5	529.3 ± 2.0	795.6 ± 31.2	114.5 ± 0.2	49.8 ± 1.8
24	49.2 ± 2.9	-378.9 ± 1.9	-861.0 ± 14.6	382.1 ± 2.0	942.0 ± 13.1	113.0 ± 0.4	94.4 ± 0.4
25	-655.9 ± 6.5	-362.3 ± 5.2	-160.0 ± 42.4	749.3 ± 6.6	766.2 ± 10.7	6.1 ± 0.4	44.9 ± 3.1
26	775.9 ± 2.2	-305.6 ± 1.6	-130.0 ± 3.6	833.9 ± 2.2	843.9 ± 2.2	80.2 ± 0.1	79.7 ± 0.2
27	1349.1 ± 1.0	-1728.7 ± 1.1	-52.0 ± 25.6	2192.8 ± 1.1	2193.4 ± 1.2	122.8 ± 0.1	122.1 ± 0.2
28	299.0 ± 5.3	-251.7 ± 4.7	230.0 ± 300.4	390.9 ± 5.2	453.5 ± 157.5	139.5 ± 0.7	128.0 ± 31.7
29	-563.8 ± 0.9	1368.4 ± 0.8	1083.0 ± 33.9	1480.0 ± 0.9	1834.0 ± 20.5	24.6 ± 0.1	56.4 ± 1.2
30	2116.5 ± 1.8	-425.9 ± 1.5	615.0 ± 12.8	2159.0 ± 1.7	2244.9 ± 3.4	27.7 ± 0.1	76.8 ± 1.0
31	300.3 ± 1.1	-44.6 ± 1.0	-64.0 ± 12.2	303.6 ± 1.1	310.3 ± 2.6	94.4 ± 0.2	77.6 ± 6.1
32	-316.4 ± 1.1	-1223.3 ± 1.5	-1185.0 ± 31.8	1263.6 ± 1.4	1732.3 ± 22.1	170.7 ± 0.1	107.6 ± 1.1

**Table B.5.** Orbit-based parameters of the 32 WBs.

Nr.	$s$ (pc)	$r$ (pc)	$a$ (pc)	$e_{\min}$	$e$	$i_{\min}$ (degree)	$i$ (degree)	$\phi - \phi_0$ (degree)	$\phi_0$ (degree)	$\psi$ (degree)	$\gamma_{2D}$ (degree)	$\gamma_{3D}$ (degree)	$\log P$ (yr)	$\log A_N$ ( $\text{m s}^{-2}$ )
1	0.0234	0.0248	0.022	0.11	0.71	19.2	53.6	321.5	14.3	81.7	91.2	105.9	5.32	-9.31
2	0.0037	0.0076	0.099	0.92	0.97	60.5	73.1	109.4	136.1	-78.2	93.4	36.4	6.40	-8.48
3	0.0239	0.0247	0.070	0.65	0.66	14.5	36.3	21.8	183.3	-73.5	89.5	81.4	6.04	-9.25
4	0.0013	0.0048	0.004	0.33	0.91	74.8	89.1	162.6	302.5	-48.2	2.2	26.7	4.19	-7.98
5	0.0180	0.0190	0.018	0.04	0.69	18.1	67.3	316.3	243.3	-52.7	145.4	107.7	5.23	-9.15
6	0.0440	0.0627	0.061	0.03	0.05	45.4	86.1	129.9	275.7	-46.8	171.8	87.7	6.01	-10.18
7	0.0014	0.0039	0.024	0.84	0.87	69.2	72.1	237.5	43.2	64.9	91.7	144.2	5.51	-7.98
8	0.0089	0.0094	0.008	0.22	0.32	18.5	34.0	145.9	248.7	-69.2	84.8	76.1	4.80	-8.80
9	0.0202	0.0281	0.017	0.67	0.97	44.0	46.9	174.3	293.6	-53.9	21.6	18.2	5.13	-9.40
10	0.0069	0.0082	0.010	0.20	0.67	32.9	78.8	297.7	95.9	-32.0	165.7	114.4	4.83	-8.37
11	0.0030	0.0057	0.007	0.13	0.24	58.2	85.7	250.2	168.3	-18.0	171.6	103.5	4.54	-8.06
12	0.0597	0.1669	0.107	0.55	0.57	69.0	84.5	172.1	257.7	-30.7	162.2	79.6	6.36	-10.99
13	0.0053	0.0053	0.003	0.69	0.99	7.2	18.7	176.1	27.0	35.8	12.3	12.6	4.08	-8.02
14	0.0047	0.0075	0.005	0.37	0.97	51.4	65.7	170.0	311.0	-43.0	13.4	16.0	4.43	-8.31
15	0.0059	0.0059	0.004	0.45	0.56	0.1	17.3	340.0	199.6	-83.3	97.4	97.1	4.25	-8.12
16	0.0011	0.0011	0.002	0.40	0.43	8.7	15.0	213.5	290.7	74.2	108.6	110.0	3.78	-6.75
17	0.0018	0.0026	0.002	0.18	0.21	45.7	50.8	335.0	92.4	-18.4	111.6	94.3	3.87	-7.46
18	0.0037	0.0054	0.029	0.82	0.85	47.0	64.2	230.1	4.2	19.2	157.4	144.9	5.55	-8.06
19	0.0098	0.0150	0.008	0.79	0.95	49.2	88.7	174.5	54.7	79.4	5.3	30.2	4.70	-8.89
20	0.0006	0.0008	0.002	0.57	0.60	35.4	72.1	215.5	2.0	-18.1	161.0	124.4	3.70	-6.30
21	0.0094	0.0094	0.018	0.47	0.96	2.4	71.1	332.6	29.9	-74.1	130.5	103.4	5.32	-8.76
22	0.0001	0.0059	0.006	0.04	0.25	88.6	88.7	114.0	336.6	-13.9	66.5	75.5	4.52	-8.24
23	0.0053	0.0198	0.036	0.45	0.75	74.4	77.9	105.5	334.7	-51.7	114.6	48.1	5.65	-9.15
24 <sup>a</sup>	0.0280	0.0281	79.158	1.00	1.00	5.1	77.9	180.0	5.2	-84.6	113.0	90.2	10.59	-9.29
25	0.0081	0.0147	0.013	0.12	0.71	56.7	85.3	142.2	160.9	-12.1	6.1	44.9	4.97	-8.83
26	0.0133	0.0133	0.014	0.04	0.18	4.1	9.3	86.9	299.5	-73.9	80.2	79.7	5.02	-8.78
27	0.0032	0.0033	0.008	0.61	0.63	8.5	11.3	205.9	202.7	-9.5	122.7	122.0	4.68	-7.53
28	0.0154	0.0864	0.269	0.68	0.79	79.7	82.6	257.1	5.7	35.9	139.5	133.0	6.92	-10.34
29	0.0007	0.0007	0.001	0.72	0.82	15.2	66.8	170.7	352.7	39.3	24.6	55.8	2.74	-6.26
30	0.0010	0.0018	0.002	0.03	0.23	57.4	75.7	96.1	203.6	16.5	27.7	76.9	3.71	-7.05
31	0.0327	0.0633	0.047	0.34	0.37	58.9	59.5	164.1	279.6	-15.2	94.3	81.1	5.82	-10.13
32	0.0024	0.0028	0.003	0.04	0.38	28.7	83.7	286.4	282.4	-42.8	170.7	108.3	4.03	-7.47

<sup>(a)</sup> Mass increased by 33%.